Rock Traits from Machine Learning: Application to Rocky Fault Scarps

by

Tyler Russell Scott

A Thesis Presented in Partial Fulfillment
of the Requirements for the Degree
Master of Science

Approved July 2020 by the
Graduate Supervisory Committee:

Ramon Arrowsmith, Chair
Jnaneshwar Das
Duane DeVecchio

ARIZONA STATE UNIVERSITY

August 2020

ABSTRACT

Rock traits (grain size, shape, orientation) are fundamental indicators of geologic processes including geomorphology and active tectonics. Fault zone evolution, fault slip rates, and earthquake timing are informed by examinations of discontinuities in the displacements of the Earth surface at fault scarps. Fault scarps indicate the structure of fault zones fans, relay ramps, and double faults, as well as the surface process response to the deformation and can thus indicate the activity of the fault zone and its potential hazard. “Rocky” fault scarps are unusual because they share characteristics of bedrock and alluvial fault scarps. The Volcanic Tablelands in Bishop, CA offer a natural laboratory with an array of rocky fault scarps. Machine learning mask-Region Convolutional Neural Network segments an orthophoto to identify individual particles along a specific rocky fault scarp. The resulting rock traits for thousands of particles along the scarp are used to develop conceptual models for rocky scarp geomorphology and evolution. In addition to rocky scarp classification, these tools may be useful in many sedimentary and volcanological applications for particle mapping and characterization.

ACKNOWLEDGMENTS

Thanks to,

Southern California Earthquake Center SCEC, Andrea Donnellan and JPL, and OpenTopography for financial support. Zhiang Chen for machine learning expertise and data processing. Chelsea Scott and Daniel Lao Davila for image collection. Duane DeVecchio and Jnaneshwar Das as committee members and mentors. Amanda Clarke for input on particle size analysis. My sister Ashley Scott for editorial support. My parents Judy White and Glen Scott for all aspects of support. Ramon Arrowsmith for advising and leading the success of this thesis and my education.

TABLE OF CONTENTS

Page

CHAPTER Page

APPENDIX

LIST OF TABLES

LIST OF FIGURES

CHAPTER 1

INTRODUCTION

A fault scarp is a displacement in the earth's surface due to faulting (e.g., Nicol et al., 2020). There are two end members of a fault scarp: bedrock and alluvial. A bedrock scarp usually exposes the actual fault plane (Figure 1a; Stewart and Hancock, 1988). On the other hand, an alluvial fault scarp is commonly developed in unconsolidated sedimentary materials (Figure 1b). There have been numerous studies that have idealized and analyzed the alluvial end member (e.g., Nash, 1984, Hanks et al., 1984, Arrowsmith et al., 1996, and many others). Alluvial fault scarps are the most frequently studied due to the relative ease in representation of the surface processes controlling their changing form over time (e.g., Hanks, 2000). Modeling the bedrock scarp end member is less common because of its physical resistance to change over time (e.g., Tucker, et al., 2011). These end members can be classified in terms of transport-limited versus production-limited scarps. The bedrock scarp in Figure 1a is production-limited, meaning its erodibility is limited by the availability of material for transport. Transportable material must be produced first by weathering (mechanical or chemical; e.g., Nash, 1980 and many others). It is more difficult for processes operating on this bedrock scarp to break up and produce transportable particles, therefore it will erode more slowly. Transport-limited alluvial scarps, however, have available loose material and their modification is limited by the ability of surface processes to transport material. As you can see in Figure 1b, it is smoother (in the upper and lower portions), there is unconsolidated material available for transport. It will change its form at a faster rate.

This research is focused on rocky fault scarps, which have alluvial characteristics. Highly fractured bedrock is faulted which enables many particles (some quite large) to quickly form and cover the face of the fault scarp. It is a bedrock fault scarp in the sense of the large particles needed to be liberated and weathered prior to significant transport. Some gross characteristics of the change in form follow the behavior of an alluvial fault scarp.

The geomorphic development of rocky fault scarps is not well explained by the end member erosion models of alluvial or bedrock scarps. The challenge is to characterize the formation, movement, and transformation of the rocks (particles) that comprise the fault scarp. Figure 2 illustrates a rocky scarp and idealizes the origin of the particles which form the scarp. Fault scarps in the study area occur within the 0.76 Ma Bishop Tuff, which is welded ignimbrite deposit and characterized by pervasive vertical cooling fractures. These primary fractures have been taken advantage by subsequent tectonic and geomorphic processes, which has led to the formation of rocky fault scarps.

Additional fractures are derived from tectonic and geomorphic processes. The tectonic fracturing is produced from the growth and offset along the small normal faults cutting the tuff (see below). Subsequent fracturing by geomorphic processes of particle impacts and thermal cycling further breaks the particles. The dominance of geomorphic and tectonic fracturing can vary over time and position along the scarp. Figure 2 shows the projection of a normal fault that will cut through the columnar joint fractures, and/or run through the pre-existing fractures (see also Ferrill, et al., 2016). In the geomorphic example, a rock, indicated by small arrows, that has been gravitationally transported down the scarp, and has broken into smaller fragments because of heating and cooling over the millennia.

Machine learning (ML) is used for object detection and classification across various disciplines (e.g., Liu et al., 2018, Bergen et al., 2019). Image-based ML algorithms can take an image of assorted items and isolate and classify each one with training. We presumed that the same strategy is applicable for particle detection along rocky fault scarps from orthorectified aerial photography. Certain ML toolkits provide positional and geometric information about the object of interest by attaching a binary mask to each pixel. Below, I walk through how ML is applied, from setup to products, and discuss how this method helped us improve understanding and analysis of rocky fault scarps by using ML to extract numerical values for each particle trait.

I have focused on simple geometric traits of the rocks comprising the fault scarp: grain size, eccentricity, and long axis orientation. I hypothesize that the distributions of rock traits along and across the scarp reflect the underlying processes and the relative roles of volcanic, tectonic, and geomorphic fracturing in the formation and evolution of the fault scarps. We test machine learning as a viable tool to accurately and efficiently collect traits for thousands of particles because manual data collection is tedious and time consuming (https://figshare.com/articles/dataset/scarp_c3_csv/12711947). Additionally, we look to improve conceptual fault models (see Figure 23, e.g. Stewart and Hancock, 1990) by incorporating rocky scarps and particle transport into the geomorphic understanding. Landform and fault scarp models are used to assess relative rates of faulting for hazard applications. Particle transport is represented by expanding McCalpin's (1993) alluvial trench model of particle classifications in which we identify additional particle types that characterize transport styles. We demonstrate how grain size represented as ϕ (-log2 of the diameter; e.g., Cas and Wright, 1988), differs along this rocky scarp and how that distribution reflects the formative processes.

Background/Location. In Figure 3, the orange area shows the distribution of the Bishop Tuff in eastern California and the N-S-oriented black lines show the distribution of an active fault array within the Volcanic Tablelands (VT) which has cut the Bishop Tuff since its emplacement (e.g., Sheridan, 1970, Ferrill et al., 1993, Pinter, 1995). The star marks the approximate location of the fault scarp examined in this study. Previous studies conducted in the region have a larger extent or different research questions, such as fault linkage processes, fault block rotation, and relay ramp evolution (e.g., Dawers et al., 1993, Peacock, 2002, Ferrill et al., 2016, Kettermann et al., 2019). The Bishop Tuff is ~150 m thick layer of a welded tuff erupted from the Long Valley Caldera ~760 ka. This area straddles a portion of the Eastern California Shear Zone (ECSZ), creating transtension and resulting in the formation and activity of the array of N-S trending normal faults. While the VT is an ideal natural laboratory for this research, the methodology presented is applicable in numerous settings where particles are detectable.

Figure 4 shows the specific images of the rocky fault scarps that I have investigated. The scarp faces are strewn with grains ranging from silt to boulder-sized particles of Bishop Tuff. Most of the scarps have a free face, or cliff forming face, at their tops. This is where we locate evidence of secondary fault surfaces or in place, columnar joint surfaces that have yet to be broken up. We rarely see the main fault surface and we can assume that between mid-scarp and the top, is the intersection of the main fault surface with the topographic surface. Most of the slope is littered with clastic debris. We call this the “debris slope” (Wallace, 1977). It gives way downhill to a lower slope area that is primarily composed of wind-blown dust. In this “wash slope,” the spatial density of the rocks (and grain size) decreases as they are transported, buried, and mixed with the eolian inputs. In an associated project with our French colleagues, we surveyed a scarp we call P13. A subset of P13 was used for this study (C3). See Figure 5 for the Digital Elevation Model we produced of P13 (see method explanation below).

CHAPTER 2

METHODS

Data Acquisition (Structure from Motion). We made several drone flights over the scarp area to produce high-resolution topography and imagery using Structure from Motion (SfM) as the first steps in the methods workflow (Figure 6) (e.g., Westoby, et al., 2012; James and Robson, 2012; Johnson, et al., 2014). Figure 7 shows the entire P13 polygon which includes 933 total images. The drone flight was approximately 75 m elevation. The coverage of the P13 area was approximately 0.9 km^2. Initially, the underlying images and the derived products for P13 used GPS positioning information from the Phantom drone which includes vertical and horizontal positioning errors. We also used 30-m SRTM data to correct vertical GPS errors (~4.74 m) and used tie-points in ArcMap basemap satellite imagery to update the georeferencing and reduce horizontal GPS errors (~2.75 m). We used UTM zone 11 throughout the processing. The image centers and overlaps are shown in Figure 7. The highest numbers of overlaps are in the south where C3 is located (our study area). The products that we primarily used for the ML are our digital elevation model which gives us 8 cm/pixel resolution. Most importantly, the orthomosaic, or our RGB or red, green, blue color values for this location, has a resolution of 2 cm/pixel. The orthomosaic is derived from the textured mesh within SfM process. The data will be published on the OpenTopography Community Dataspace (Scott, et al., 2020; https://doi.org/10.5069/G9SF2TC5).

Figure 8a is the orthomosaic of P13 showing the RGB orthoimage. The background of Figure 8b is the digital elevation model for the entire site, however, the green and purple colors represent the elevation model for where the ML analysis was done (C3). The orthomosaic in Figure 8a was the basis for the machine learning segmentation and rock trait identification.

Field Validation. I visited the field site twice. The first time was in support of additional drone surveys. The purpose of the second visit was to collect field data to compare with the ML results. I measured the grain sizes, long axis orientation, and eccentricity of a subset of rocks on the P13 scarp. Caution tape was used to mark off a 5-m wide slot across the fault scarp (Figure 9). The length of it stretched from the wash slope to above the scarp until I found no significant rocks. I conducted this process in two locations for a total of 680 particles (Figure 9c and 9d). Only one of the sites overlapped with C3 or the ML results (see Results section; Figure 22). I examined each rock within this taped area, considering the vertical perspective of the ML analysis on the orthophotos. The key in this evaluation is to measure all of the rock traits from the top down view. This is not the easiest or most precise method of measurement, but it is important so that the data sets were comparable. I began by drawing a chalk line down the long axis and measured its length and orientation (Figure 9b). I used a mobile app called “Field Move.” I measured the horizontal projection of the long axis with a tape measure and its orientation using the built-in compass in Field Move. The positions were automatically measured and recorded from the mobile phone GPS. All information was stored digitally in a Field Move database and exported for plotting in ArcMap.

Machine Learning. Measuring the rocks in the field is time consuming, tedious, and there are also precariously stacked rocks. Navigating in the field over the rough terrain can be risky and there are tens of thousands of particles along the scarp. Measuring and collecting large volumes of rock trait data is very labor intensive. One of the key questions is: "if a Geologist can identify these rocks in the field or more specifically from an image on a computer in the office, than can this ML do it as well?"

We used what is called a Mask – RCNN (He et al., 2017, Chen et al., 2020). A Mask-RCNN or RCNN stands for is region-convolutional neural network. Previous implementations would create a bounding box around an object and use linear regression to fit the box around the object. A Mask-RCNN integrates a fully convolutional neural network (Figure 10). Each one of the gray circles represents a node, where there is the input, hidden and output. The arrows define what a fully convolutional neural network means; in every proceeding layer, whether it is hidden or not, the output is influenced by each of the previous inputs. Every node prior is linked to the following node. They all communicate. What happens in this hidden node is the ML of these meta algorithms, just one example, is they geometrically manipulate these images. It could be in a square shape, but these algorithms may distort it and look at it from different angles and create a rectangular shape instead. The mask is not just the bounding box information, but now we have information for every pixel. Each pixel within this bounding box gives it a value of a 1 if it identifies it as a rock. It then works outwards and can cluster each of these pixels and group them to form the complete identity of a SPECIFIC rock. It knows it has reached the edge of a rock based on color or texture variations of the pixels. If it is not a rock, it gives it a value of 0, because there is no rock present. This binary mask provides information for each pixel that composes each rock.

To begin machine learning setup, we *teach* the computer what a rock is. Figure 11 represents a tile from C3. We broke up C3 into tiles with each tile having dimensions of 400 x 400 pixels. The operator then clicks out a polygon or a bounding box around each rock using the "Label Me" tool (https://labelsnicheideas.netlify.app/label-me-github.html) and assigns the polygon a classification. For this study, there was only one classification: rock. The application assumes that if you did not classify it, it is not a rock. There were 45 tiles that were annotated out of 1755 tiles that made up C3. After training the ML, then it is necessary to *test*. This is not a full application of the ML. For example, if you annotate 45 tiles, and because you have annotated the rocks that you can assume that these annotations are perfect, you then out of that 45 withdraw possibly 10 of the annotated ones and you run this small subset of training as a validation test. Run the small subset of rocks through ML. The ML output for those tiles is compared with the ML output. If the correspondence too low, more annotation is needed followed by additional testing.

While doing my annotations, I found the occasional bush obscuring a rock (Figure 11). In this case, because there was a rock projecting under a bush, I would estimate the rock boundary to the best of my ability. If I could not see a rock, or it was a rock completely obscured by vegetation, there would be no rock mapped in that instance. Fortunately, the scarps are not heavily vegetated.

After we annotated and tested, we *trained*. The network was setup and run through the data set of C3 on all 1755 tiles (Figure 12).

Post machine learning, significant processing was required to compute the rock positions and traits. First, the mask might have a hole (purple line, Figure 12a). We generate contours or boundaries within the mask (green line; Figure 12b) (Chen et al., 2020). We assume that there are no torus-shaped rocks. The outer most contour defines the rock, completing the mask and uniquely separating the resulting rock polygon boundaries (Figure 12d).

Secondly, when we created these tiles, the tile borders cut through some rocks. This would sometimes split one rock which should be connected, but because of the tiling strategy, it would then say that it was two rocks because it is two different tiles. The rocks were stitched together across the boundaries.

Finally, we computed the rock traits (Figure 14, see Table 1 and Appendix 2). Because the computations were performed on the georeferenced orthophotograph, the ML mask provides us positional information for rock polygon. From them, we computed the upper left coordinates and used that as the rock position.

The area of the polygon defined the horizontal slice through the rock and was the direct measure of grain size in square meters. From that area, we computed a more traditionally used equivalent grain diameter in millimeters:

$$d = 2\sqrt{\frac{area}{\pi}}1000 \qquad (1)$$

and from that, the standard size scale (e.g., Cas and Wright, 1988, Appendix 1):

$$\phi = -log_2 d. \qquad (2)$$

Grain size distributions are commonly analyzed for sedimentary and volcanic particles and provide information on characteristics of the depositional process (Visher, 1969, Cole et al., 2002). Varying ϕ values are associated with different grain size names. A ϕ value less than -8 is a boulder and a ϕ value of -8 to -6 is a cobble. That grain size range is the most relevant for the C3 statistical analysis of grain size distribution. With the ϕ value we can summarize the grain size statistics (Figure 15) to represent the median diameter (Md_ϕ) for a given area, along with its standard deviation (σ_ϕ), and the asymmetry of the distribution (α_ϕ).

$$Md_\phi = \phi_{50} \qquad (3)$$

$$\sigma_\phi = \frac{\phi_{84}-\phi_{16}}{2} \qquad (4)$$

$$\alpha_\phi = \frac{[(\phi_{84}+\phi_{16})-Md_\phi]}{\sigma_\phi} \qquad (5)$$

The median grain size for C3 is -8.77 (Figure 15c) which is consistent with boulder size classification. The histogram of ϕ in Figure 15d graphically spreads out the distribution and shows us the ML does not detect particles below the cobble classification bounded by ϕ = -6.

We fit ellipses to the bounding rock masks (Figure 13). From that the principal axes (long a and short b) provide the eccentricity

$$e = \surd(1 - a^2/b^2) \qquad (6)$$

The ellipse long axis also has an orientation which is the final trait we analyzed. We note however, that the long axis orientation is not well defined for small eccentricities.

Table 1

Rock traits from ML. These traits include the upper left (NW) location (UTM zone 11 Easting and Northing in meters), horizontal area (m^2), orientation of long axis (clockwise from north), and the eccentricity (equation 6). See the Appendix II for the entire 12682 particle dataset. https://figshare.com/articles/dataset/scarp_c3_csv/12711947

rock id	UTM easting (m)	UTM Northing (m)	Particle horizontal area (m^2)	Orientation of long axis clockwise from north (degree)	Eccentricity (eqn. 6)
0	372441.6	4146069.4	0.110	128.3	0.69
1	372441.1	4146063.8	0.038	83.3	0.17
2	372441.1	4146064.0	0.032	90	0.02
3	372441.0	4146063.6	0.046	72.2	0.78
4	372441.5	4146063.1	0.060	91.8	0.71
5	372440.7	4146063.2	0.030	81.2	0.62
6	372441.2	4146066.5	0.192	83.9	0.71
7	372442.0	4146068.4	0.141	160.7	0.46
8	372441.9	4146069.6	0.092	81.3	0.64
9	372440.1	4146064.2	0.056	81.6	0.79
10	372438.4	4146063.8	0.025	97.3	0.66

CHAPTER 3

RESULTS

C3 Statistics. First, I present an initial analysis of the particle statistics for the entirety of C3. Within C3, the ML detected 12,682 rocks whereas when done manually, it took 1.5 – 2 days to measure 680 rocks (Figure 14). Figure 14a is a representation of the scarp where there is a black dot for each particle. The particle detection on its own can serve as a mapping technique for the scarp. Figure 14b is a particle size distribution histogram. We can see that there is a peak occurrence around 0.2 m^2 for particle horizontal area (0.5 m equivalent diameter or ϕ = -8.98). The rollover in frequency of the smallest particles does not indicate necessarily a lack of smaller grains, but rather suggests a decrease in sensitivity. As we start to get into the terrain of rocks that are too small, they are either undetectable by ML for training reasons, or the resolution of our imagery (2 cm/pixel) does not go down to the size of these rocks. The sensitivity to smaller particles remains a significant limitation with this dataset.

The peak in eccentricity is ~0.7 (Figure 14c). On the left is an eccentricity value of zero, meaning a perfect circle (Figure 14c; eqn. 6). On the right is a very elongate rock. For reference, an American National Football League football is 27.9 cm wide and 55.8 cm long. That yields a cross-sectional area of 0.16 m^2, an equivalent diameter of 0.45 m, a ϕ of -8.8 and an aspect ratio of 0.5 (in other words, fairly similar to our modal detected grain size).

There is not a strong preferred particle long axis orientation (Figure 14d). The mode is about 0-030. The scarp in general has a N-NW trend. Given the relatively elongate particles (0.7 eccentricity), we expect these particles to roll down the hill like a football, giving us an expected 350 degree trend for the long axis orientation. However, we do not see that for all of the particles but more of a uniform distribution suggesting that rolling transport is not controlling particle orientation.

Granulometry (Figures 15 & 16) provides insight into grain distributions. As particle frequency increases along the scarp, we see an increase in $Md\phi$ and $\sigma\phi$. However, $\alpha\phi$ commonly decreases when these other ϕ values increase. The 4-meter sampling along the scarp (Figure 16a) mostly samples sufficient particles for reasonable statistics but also provides a detailed presentation of the variation of those particle traits (Figure 16b). $Md\phi$ and $\sigma\phi$ behave similarly with similar peaks in small particle abundance (Figure 16c, d). However, $\alpha\phi$ behaves inversely.

Further analysis of the particle distributions along and across the scarp begins to show interpretable variation (Figure 17a). The illustration highlights the relay ramp around 310 where the northern linking scarp segment curves while the southern linking segment is straight. Figure 17b aligns the 4 m samples on the scarp center. $t$he majority of particles are near the center of the scarp (Figure 17 d, e). We see primarily small ϕ particles at the top of the scarp (left) likely because the columnar joints are exposed but still in-tact which are not detected as particles. It is also possible that the steeper upper scarp rids large particles quickly. Small ϕ particles dominate the lower scarp. As particles move down the scarp they smash into other particles and break into smaller pieces which is one input. Also, by the standard of particle sorting we expect the smaller particles to travel further. The smaller particles can fit through cracks and voids as they move down scarp while larger particle may hang up on one another. ϕ analysis on all C3 particles does not show a clear particle alignment preference even when eccentricity is greater than 0.5 (Figure 18). Analyzing particles where ϕ is greater than -7.7 (smaller particles) shows that small particles are most frequently detected on the scarp perimeter (Figure 18f). This does not mean small particles are not present mid-scarp but possibly lie within the cracks between large particles and are therefore concealed. There is a clear preference in axis orientation for small particles at NNE and SE (Figure 18h, j).

Specific Sites. I identified several representative locations along the C3 scarp to examine the map and statistical patterns of the rock traits (Figures 20, 21). We review two distinct scarp forms with the first example being a “typical rocky scarp”. This example does not have any outstanding geomorphic patterns relative to most of the scarp and for that reason it is typical. The typical scarp is the baseline for pattern comparison to other geomorphic examples (see Figure 19). The second is an example of a relay ramp (figure 21d). One of the most distinguishable geomorphic patterns we come across is the axis orientation discrepancy for the relay ramp.

The rock trait diagrams for these sites show some pattern consistent with the different zones along the scarp. In Figure 20a, the particle size distribution peaks at 0.2 m^2 and drops off quickly as particles get larger. In Figure 20g, in the red, the free face is characterized by a greater abundance of small clasts relative to larger clasts. Large clasts are seen farther down in the wash slope and small particles are less frequent. Smaller rocks are there but the sand has covered them. Figure 20d shows a scarp parallel preference of long axis orientation.

The relay ramp defines the linking point of two normal faults and shows associated geomorphic properties (Figure 21). There is a 0.7 peak in eccentricity and another peak around 0.55 (Figure 21c). The long axis orientations (Figure 21d) are unusual because there is northwest and a northeast preferred orientation, possibly due to the slope directions of the ramp versus slope directions of the fault scarps. Figure 21g shows the ramp in the blue where we can see a lack of larger rocks in the ramp compared to the scarp faces. It is possibly because this area has not been fractured as much and the free face has not breached the upper ramp. However, there is a line of large rocks across the upper ramp which might imply an early stage evolution of a breach.

CHAPTER 4

DISCUSSION

Field Validation. Comparing field collected data with the ML results is essential. We need to have external control on the quality of the ML process. However, our rather limited field validation is only able to support the ML results in a general sense. The frequency of particles detected differs in Figure 22 where n=177 for ML and n=225 for field. The increased count for field measurements is due to the human ability to measure smaller particles in the field that are not detectable in ML due to resolution limits. There is not a good correspondence between the orientations of the long axes (Figure 22a) which is likely from the discrepancy due to smaller particles potentially biased from increased roundness relative to that inferred from the ML. The particle locations scaled by their areas are shown in Figure 22b. The finer spatial scale here causes a problem because of a mismatch between the positioning of the orthophoto (with its georeferencing) relative to the mobile phone GPS that was used for the field positions. Not only do the individual particle locations mismatch, but the position relative to neighboring rocks do not align.

I recommend a differential GPS system be deployed to acquire positions for rocks in the field with only decimeter errors compared to the meter errors we experience here. In addition, manual mapping of the particles on the orthoimagery would enable direct comparison with the ML results.

Conceptual Models. We advance the block model concept from Stewart and Hancock (1990) to incorporate our rocky scarps (see Figure 1). Their models include a detailed piedmont scarp along with other complex evolutionary fault models such as splintered or multiple scarps with associated geomorphic implications. These models are useful for reference when trying to assess fault scarp processes and evolution of scarp form.

I developed a series of models based on the patterns in the ML results and my field work (Figure 23). They range from predominantly production-limited on the left to transport-limited on the right. There are scarp forms dominated by a free face (Figure 23a). There is minimal debris slope due to a lack of sediment production, which is indicated by the ML as an area where there is less rock detection. Figure 23b is our typical example for when we see the appearance of a free-face, a wash-slope, and a debris-slope. Here we can map and better understand the particle evolution (Figure 20). There are areas where we have just a debris-slope (Figure 23c); the free-face is nonexistent. Particle sizes, possibly set by distributed volcanic or tectonic fracturing as well as eolian input, are diminished. The ramp (Figure 23d) developed in a scarp segment of two merging faults with slightly different orientations. In Figure 23e, the lower portion of the scarp profile projects above the top of the scarp. This may be a two-fault system in which this lower fault was active in the past. Later, the second, eastern fault was activated, following pre-existing volcanic fractures.

Particle Transport Modes. Seminal work by McCalpin, et al. 1993 on particles in colluvium on alluvial scarps inspired me to modify their sedimentological model derived from epoxy castings along trenches in fault scarp colluvium, Borah Peak. They measured clasts and classified them with a name where each name implies the transport mode. The Stacker, the Herringbone, the Slider, and the Sideways Roller (Figure 24) are modes that McCalpin was able to observe in the Lost River Fault alluvial scarps (Table 2). A Noob is a rock that has been fractured and slightly separated from its larger parent rock. The Splitter is one rock that is now two. Soon it will be mobilized. The Shim is wedged between different rocks. Its evolution is dependent upon what the rocks surrounding it do. The particle orientations along C3 slightly favor a sideways roller, defined by McCalpin, where the long axis is scarp parallel. However, this assumption is based on orientation plots and is not yet visually confirmed across the map.

Thermal cycling (McFadden et al., 2005) will change particle axis orientations without transport and may provide insight into the abundance of axis orientations that are not scarp parallel. McFadden’s work in the region showed a N-S trend because of insolation which is consistent with the orientation trait (as opposed to scarp parallel). The angularity and potential disruption signal from faulting events set a wider distribution of particle orientations. We can assume that an increased duration with only geomorphic influence will show dominance in the orientation signal.

Table 2 (New terms expanding McCalpin 1993)

Particle transport clast types (See Figure 24)

Name	Geomorphic Meaning
Noob	Dislocated from in situ parent, not yet remobilized
Shim	Trapped by other particles, evolution is dependent on neighbors
Splitter	Mobilized particle that is split but not separate until mobilized

Machine Learning and Extension of the Interpretations of Fault Scarp Processes. The Mask-RCNN tool is sufficient for detecting and isolating particles that are densely strewn along a fault scarp face. The ML application allowed us to isolate thousands of rocks and extract traits for each one. That result alone is not achievable with a field campaign. Additionally, the ability to manipulate the ML data for granulometry allows us to test ideas about scarp evolution. However, a geologist needs rigorous training or experience with ML algorithms along with various software tools and programming packages. The ML application in this thesis incorporates collaboration with robotics and computer scientists to develop and refine the method.

The next step to advance ML in this scenario is to improve validation methods and consider a 3D application to understand the processes controlling the development. A controlled lab study would allow us to precisely measure, validate, and refine the current performance. An example is to build a model rocky scarp made of dice where the size and orientations are exact and lead to the exposure of specific ML flaws. Computer simulations (e.g. Tucker et al., 2018) and physics engines for gaming environments (e.g., https://www.ode.org/) are available for particle dynamics modelling. These computer modelling techniques will assist in working forwards or backwards on particle transport evolution modelling along with exposing statistical probabilities for particle locations.

CHAPTER 5

CONCLUSION

Rocky fault scarp geomorphology and evolution processes are better understood and easier to assess because of ML. We hypothesized that if we can identify these rock traits and use ML to detect them, can we then go back and use this information to apply to better understand rocky scarps? Are we able to determine the difference between bedrock and alluvial scarp evolution? ML provided us with statistical information for particles that we can use for rocky scarp analysis. We have shown that ML allows us to take a seemingly chaotic assortment of thousands of particles and collect individual particle traits using granulometry and ϕ transform that lets us examine the spatial variation of particle size on the scarp. We were able to bridge the gap in alluvial and bedrock scarp studies to improve how transport-limited and production-limited processes coincide and advance upon previous scarp conceptual models. Application of the ML products shown in this thesis will advance hazard assessments in terms of semi-autonomous mapping can unveil previously unmapped fault scarps. Additionally, we relate particle transport evolution to the geomorphic configuration of the rocky scarp enabling us to anticipate how current segments will evolve or move in upcoming earthquakes.

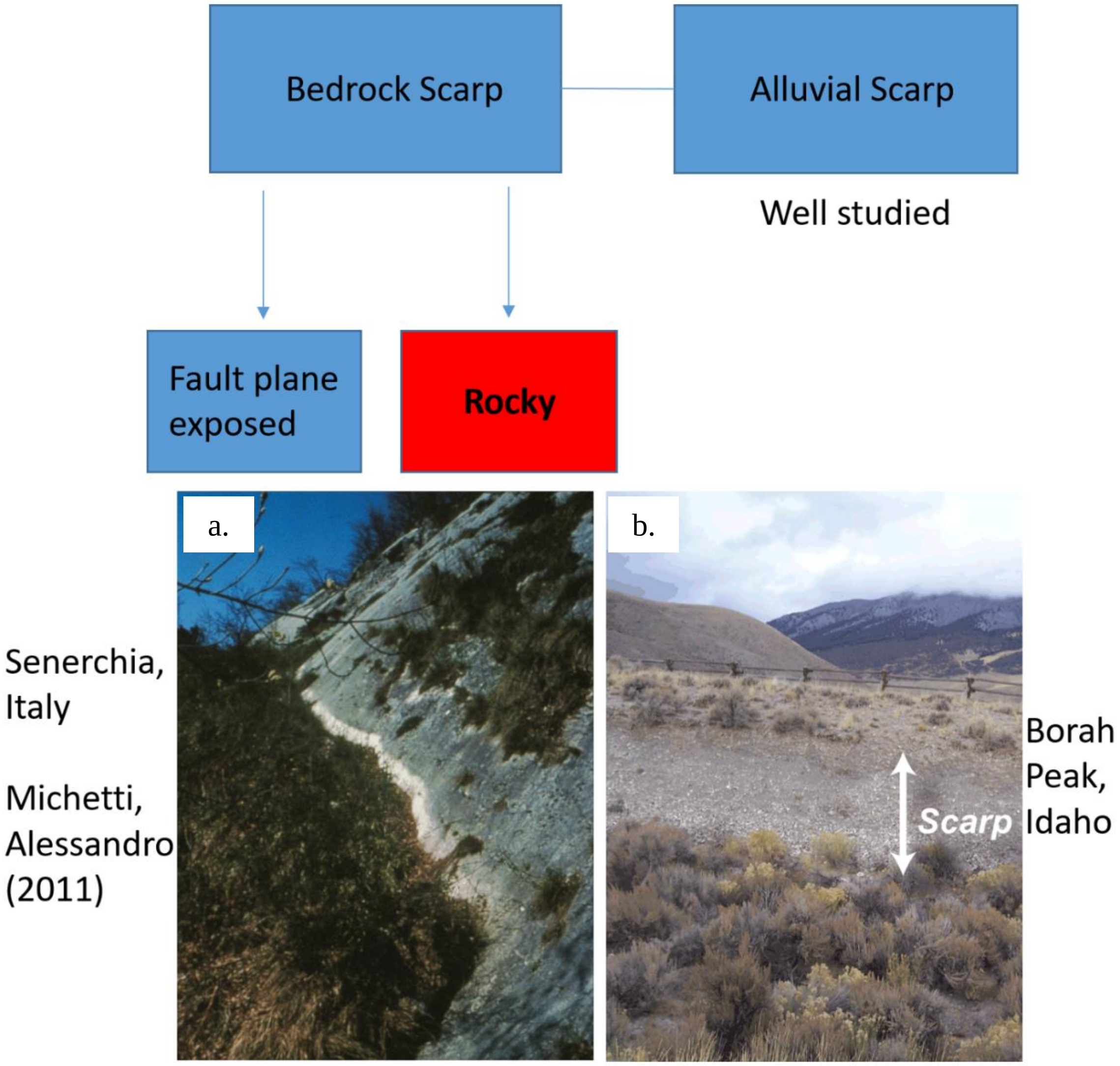

Figure 1. Flow chart showing end member bedrock and alluvial fault scarps and other scarps within the hierarchy. Rocky scarps—the topic of this thesis—are an intermediate position conceptually. (a.) Bedrock scarp with fault place exposed. (b.) Alluvial scarp.

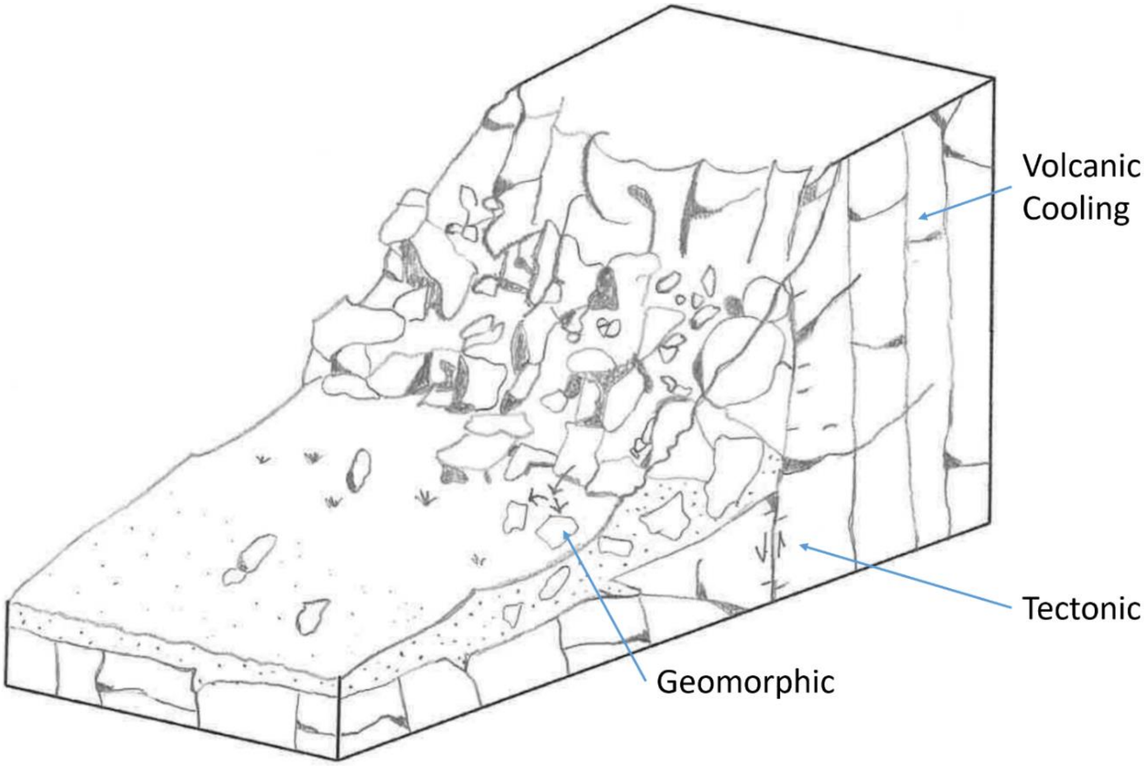

Figure 2. Conceptual model of a typically observed normal fault scarp in the Volcanic Tablelands (Figure 3). In situ columnar joints may be further broken by faulting and then break into rocky particles and fall down slope. Dust blankets lower topography. Three modes of fracturing control the production and traits of the particles on the scarp: volcanic cooling represented by columnar joints, tectonic represented by normal fault-related deformation, and geomorphic represented by collisions and thermal cycling.

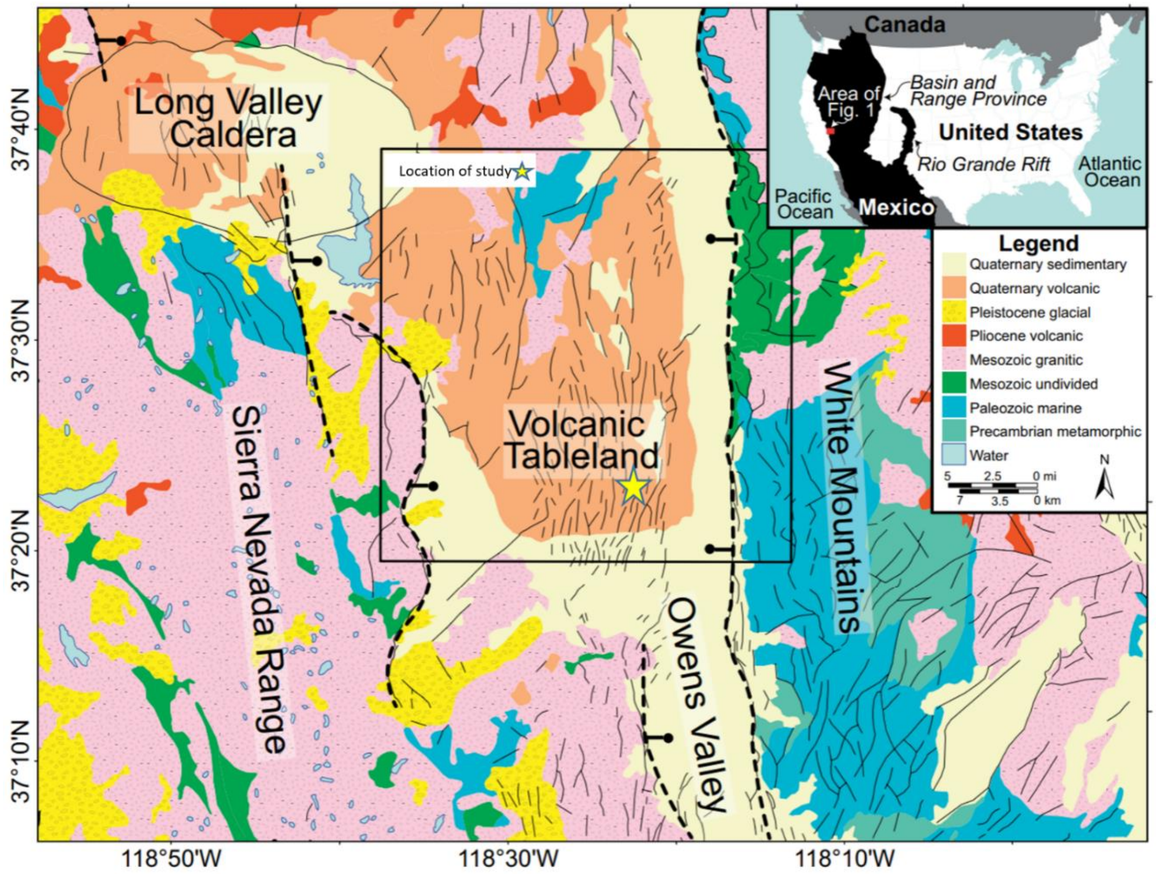

Figure 3. Mapped normal fault array (modified from Ferrill et. al, 2016) within Eastern California Shear Zone (ECSZ). Thesis data location marked by a star within Volcanic Tableland (see Figure 4).

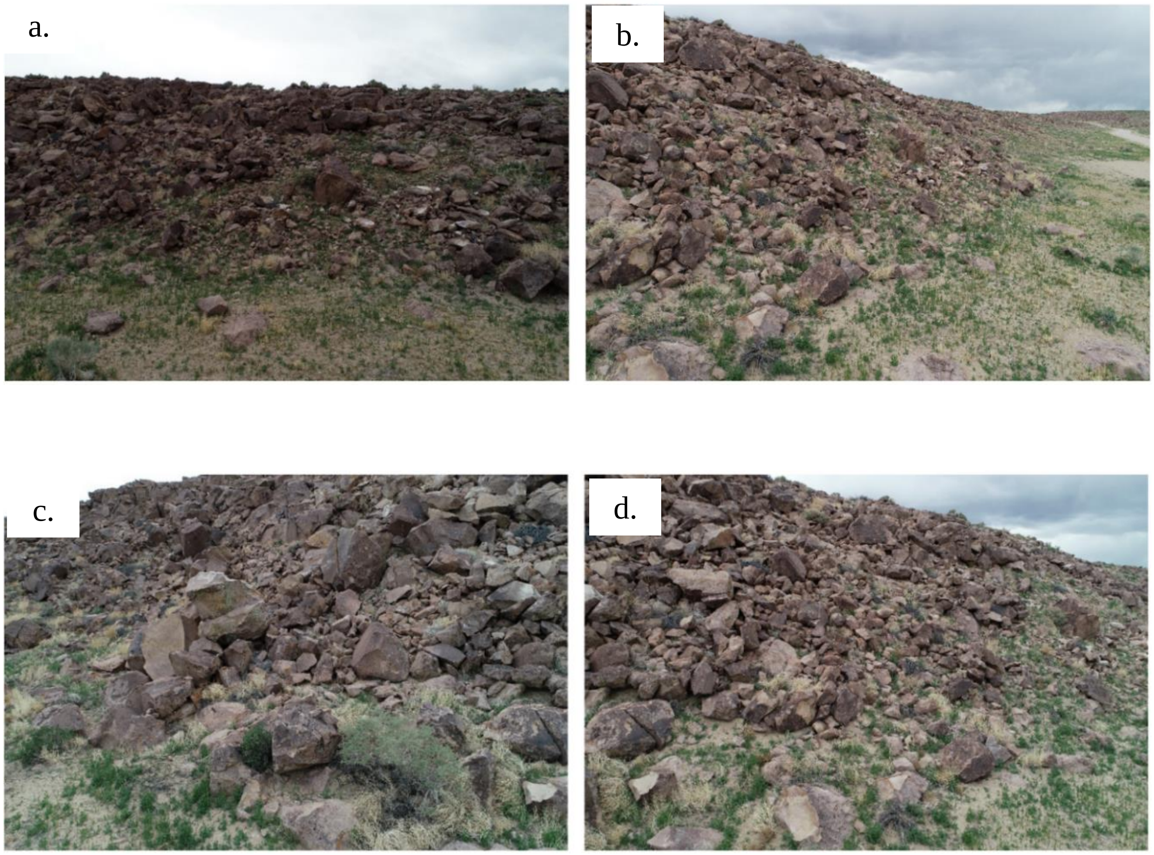

Figure 4. Field photographs of a normal fault scarp (in the C3 survey) that is approximately 5-12m high. Commonly observed is a more resistant upper face transitioning to a moderately sloping mid scarp strewn with poorly sorted angular particles ranging in diameter from centimeters to two meters. The lower slope is subdued due to an influx of windblown dust. Photo locations in Figure 7.

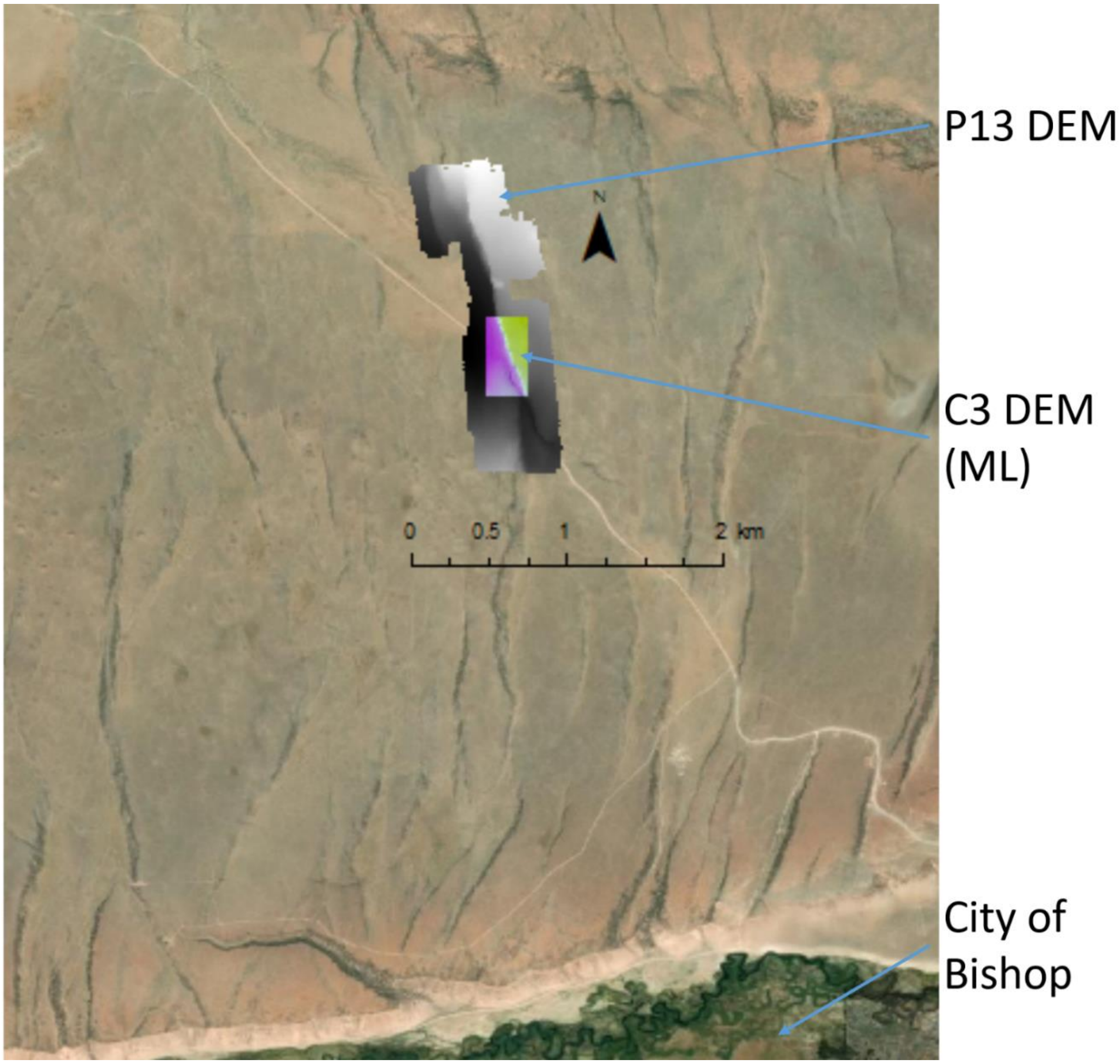

Figure 5. Satellite imagery basemap of Volcanic Tableland plateau including the entirety of P13 fault scarp DEM, C3 DEM used for machine learning analysis (ML), and proximity to the city of Bishop.

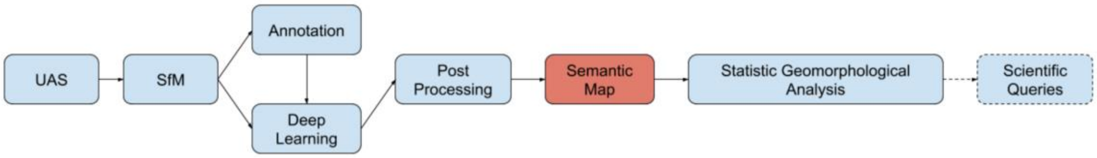

Figure 6. Methods workflow diagram (from Chen et al, 2020) with initial image acquisition from drone (left) leading to statistical analysis of numerical data for individual particles (right).

Survey Data

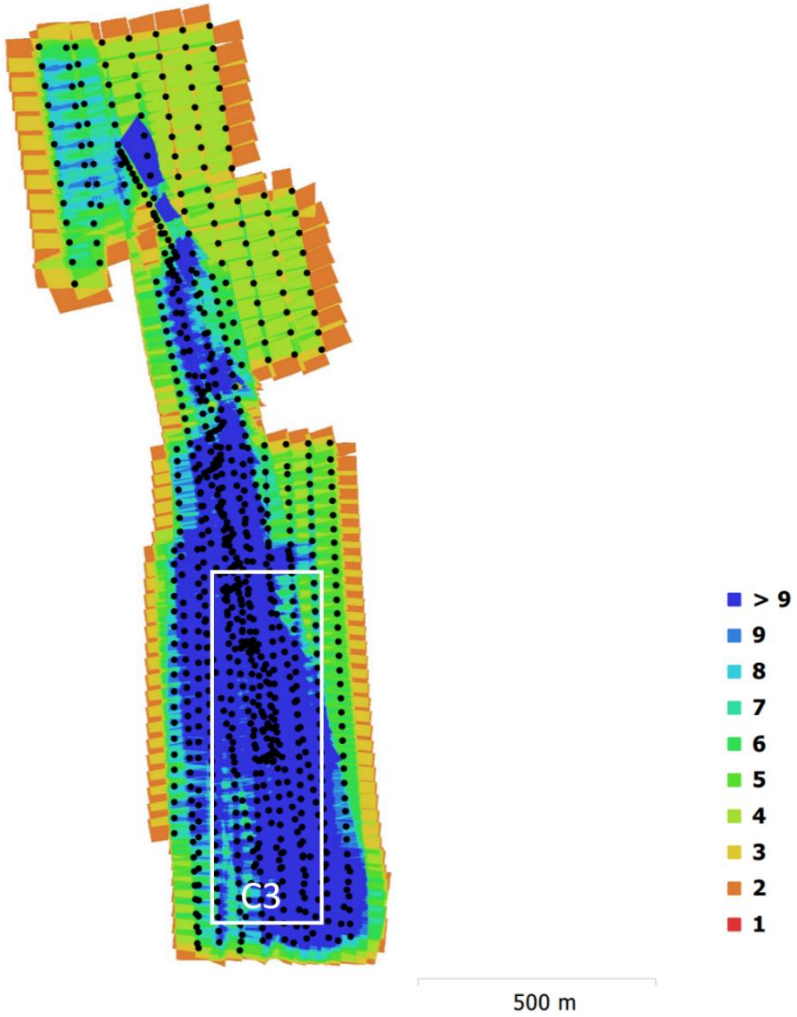

Figure 7. Coverage map of P13 from drone campaign where the dots represent camera locations and the heat map corresponds to image overlap, where blue is maximum overlap.

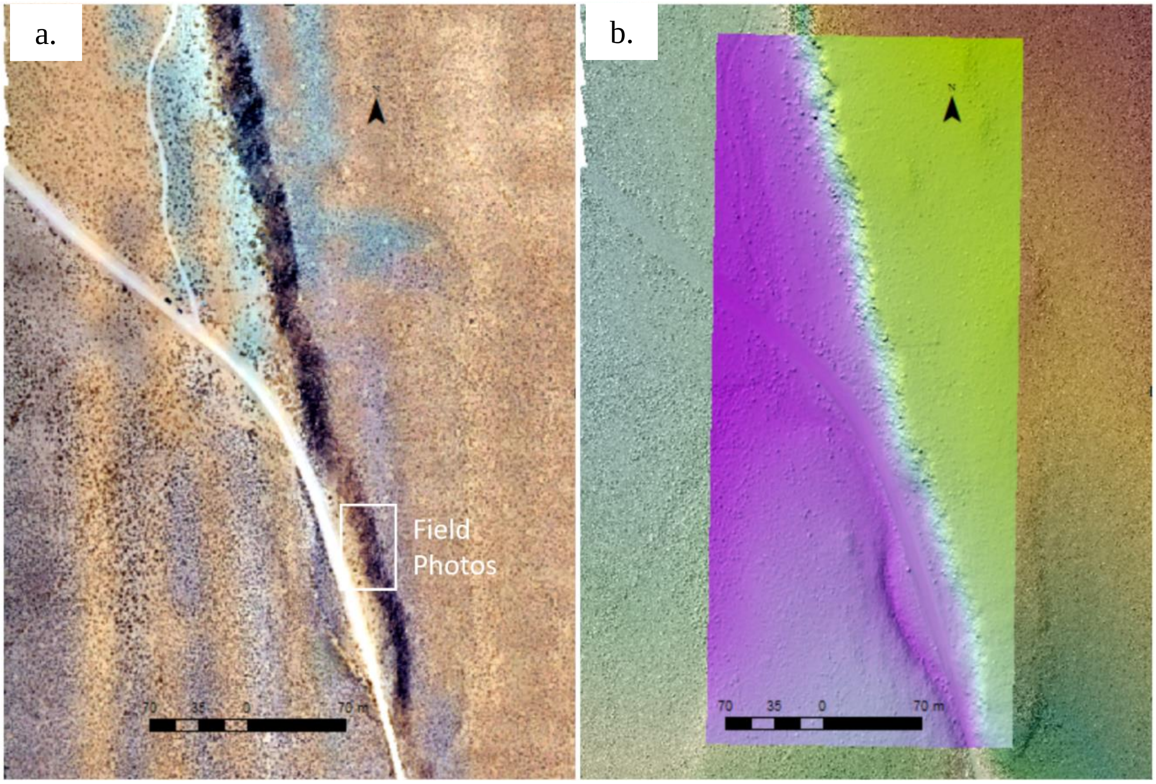

Figure 8. Structure from Motion products of identical locations (C3). Field photos location for field validation, Figure 9. (a.) The orthomosaic (2cm/pix) which is composed of RGB values derived from the textured mesh (corrected for topography). (b.) The digital elevation model (8cm/pix) derived from the dense point cloud.

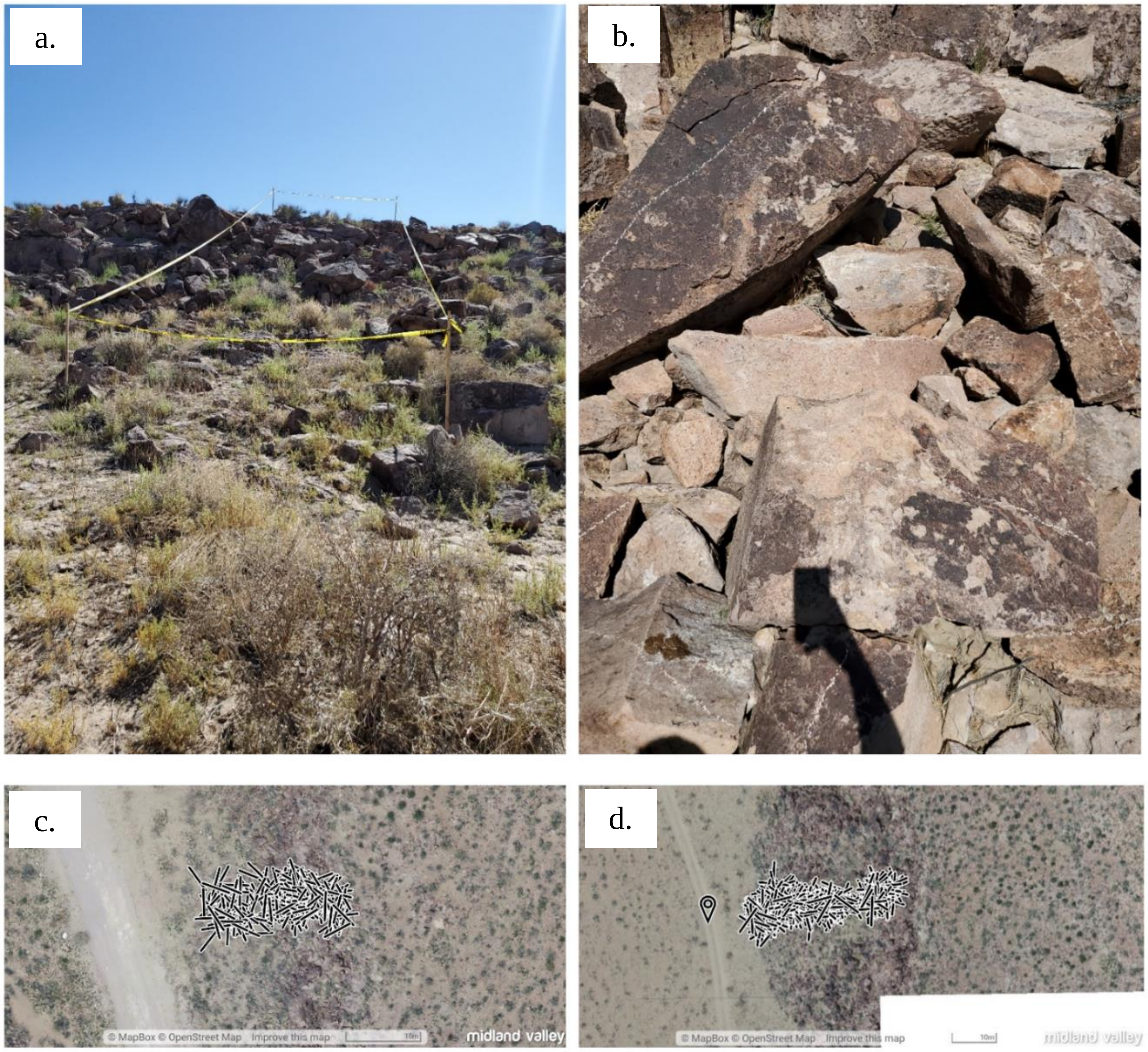

Figure 9. Field validation campaign represented by field photographs and digitally mapped features. (a.) 5m wide swath across the scarp bounded by caution tape within which the rocks were measured. (b.) Illustration of how the long axis of each particle was chalked to indicate the top down view for correspondence with the machine learning outputs. The chalk lines helped to avoid repeat measurements. (c.) A map of digitally stored rock measurements with positions and axis orientations plotted. This site lies within the machine learning area. Photo locations in Figure 7. (d.) Same approach as (c.) however, lies outside the machine learning area.

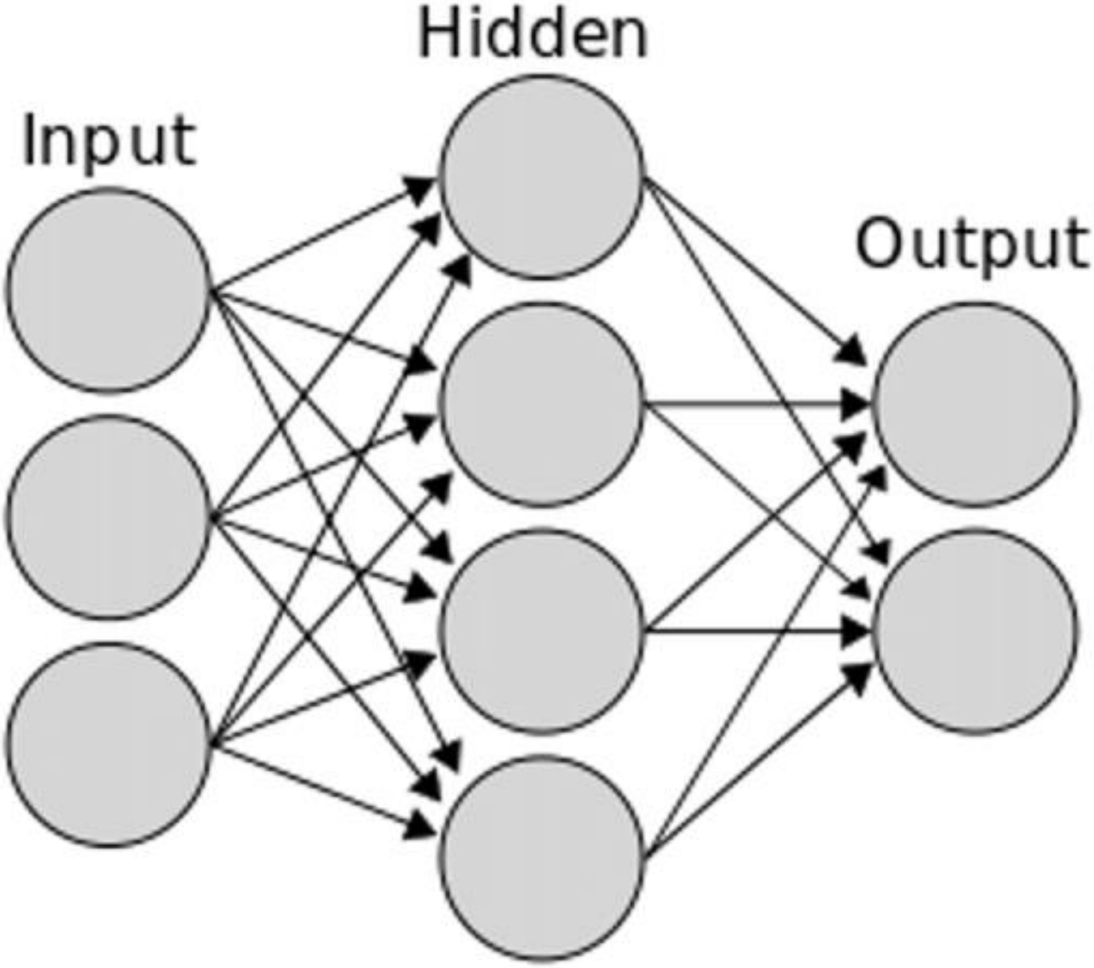

Figure 10. A conceptual model of a fully convolutional neural network. Each gray circle represents a node and each arrow represents node communication. Each node has some path of communication with all other nodes. The input nodes will be our image. The hidden nodes are image manipulations conducted by meta algorithms and the output nodes are the mask. (DeepMind, 2018, https://fold.it/portal/node/2008706).

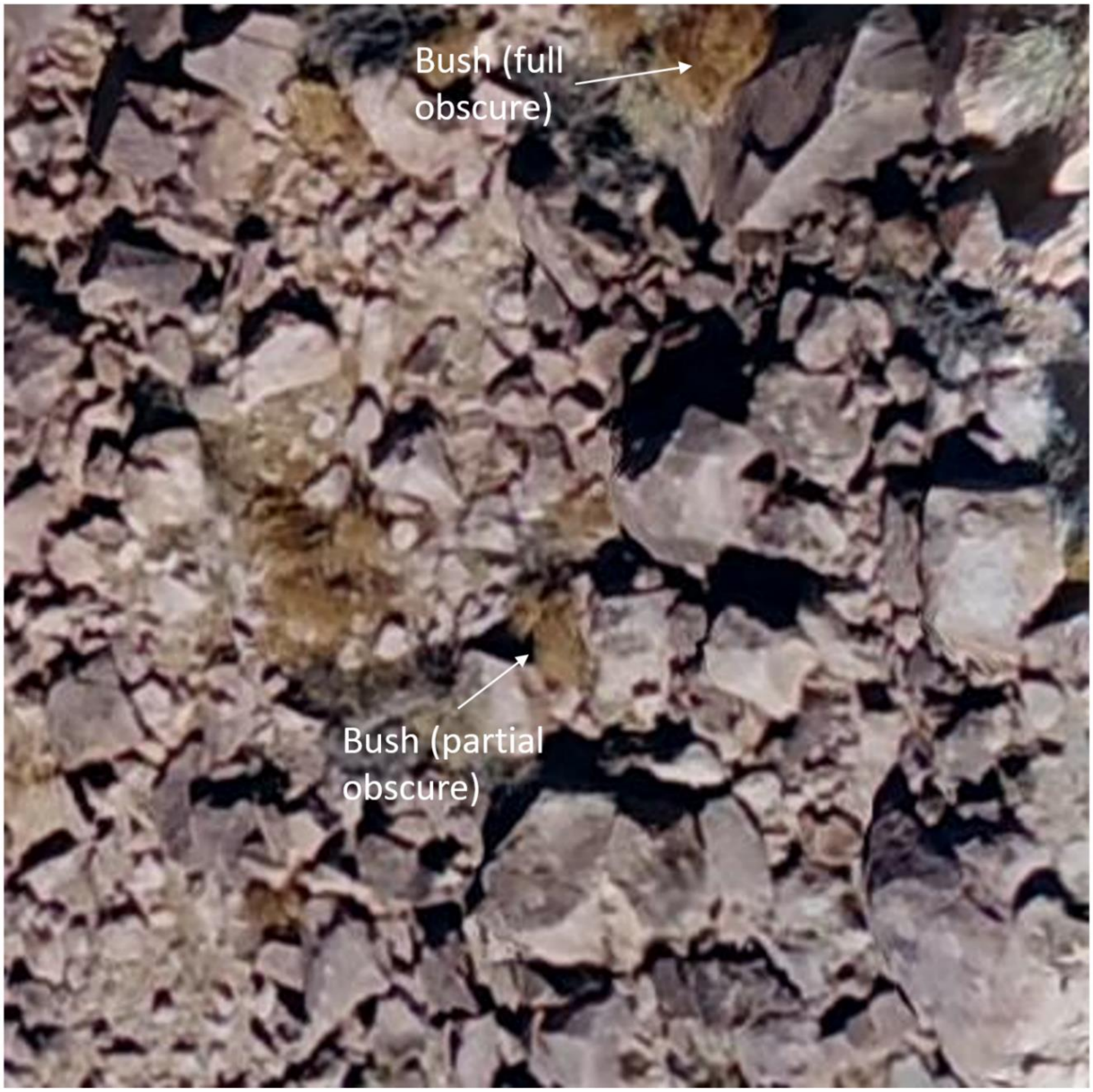

Figure 11. This is a tile cut from the orthomosaic that was used for machine learning training. Each tile is 400 x 400 pixels wide (8x8m).

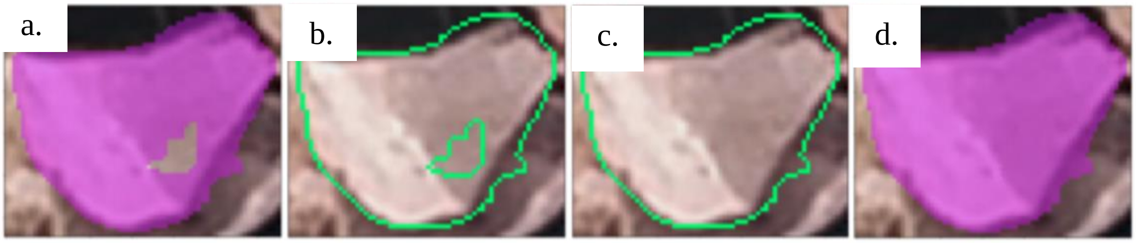

Figure 12. Machine learning post processing. This figure shows how the machine learning inferred a rock with a hole and how the outer boundary was kept. (a.) Mask of a rock with a hole in it. (b.) Shows how the machine learning produced two sets of contours, therefore, two rocks. (c.) Post processing resolve for contour error by removing the inner contour. (d.) Accurate mask is fit to the correct outer contour (Chen, et al., 2020).

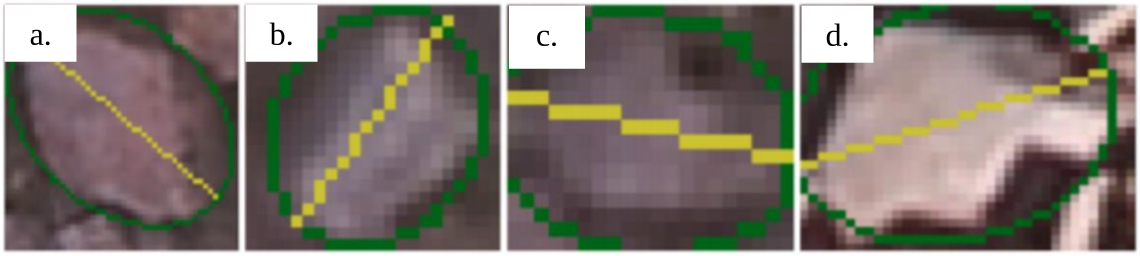

Figure 13. Ellipse and long axis orientation extraction from post processing. The green line shows the best fit ellipse boundary while the yellow line shows the corresponding long axis fit. These provide the rock area, eccentricity, and long axis orientation traits (Chen, et al., 2020).

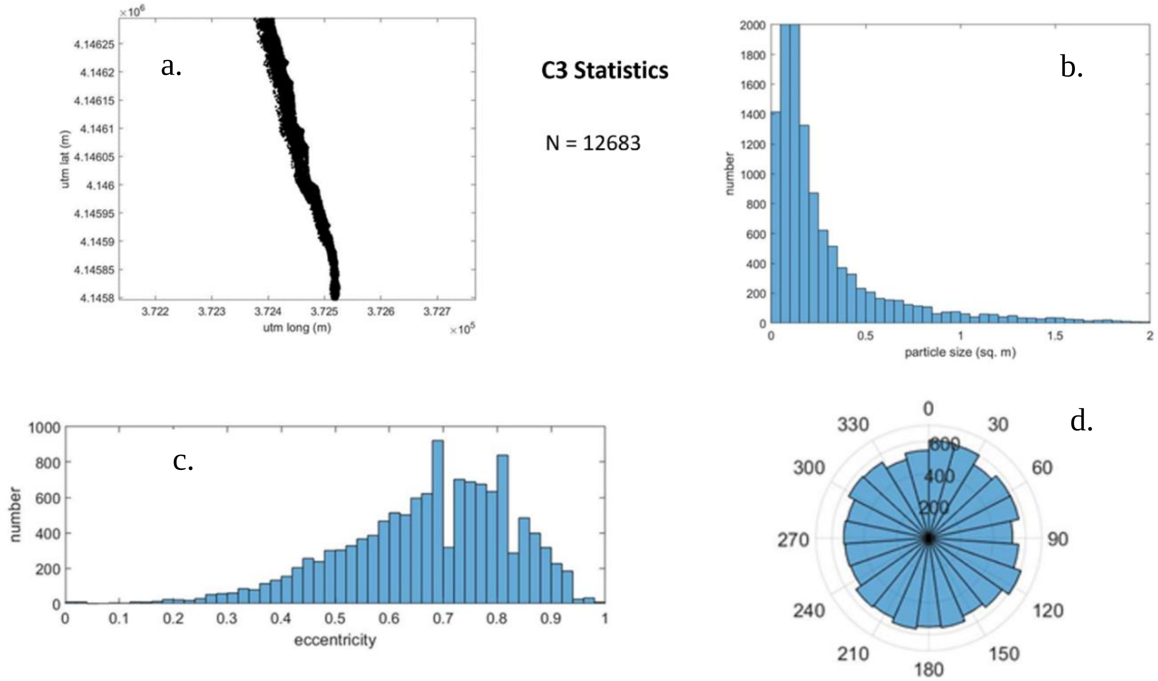

Figure 14. Particle statistics for the entirety of C3. (a.) Black dot in the location where a particle is detected. (b.) Particle size histogram where particle size is on the x-axis, which was cut off at 2 meters for neatness, and frequency is on the y-axis. (c.) Eccentricity histogram where eccentricity is on the x-axis. A value of zero is a perfect circle and elongation increases towards 1. (d.) Long axis orientation rose diagram where zero is North.

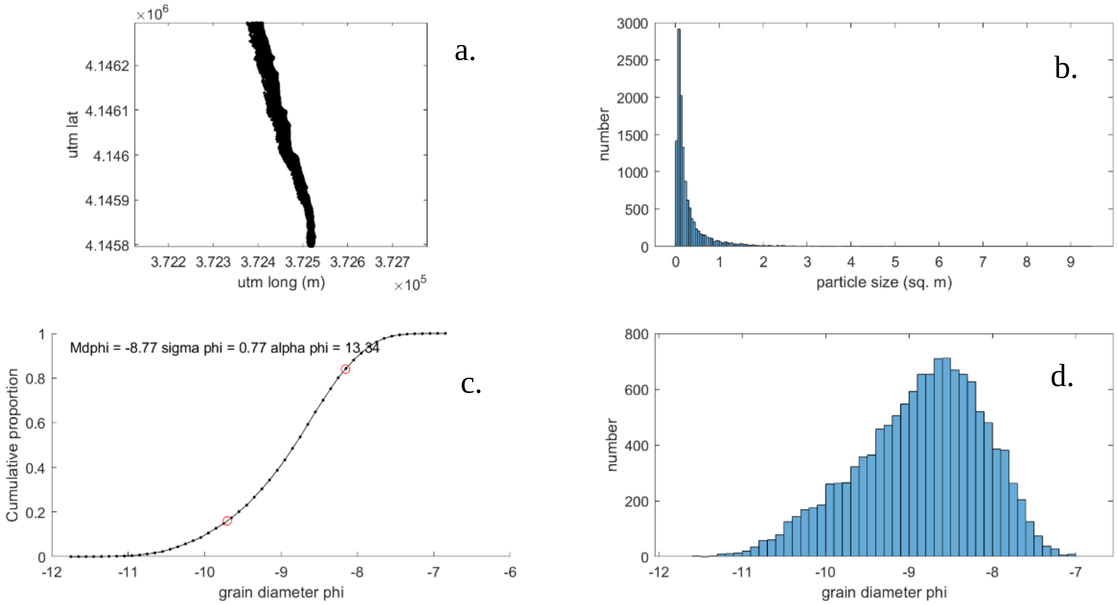

Figure 15. Analysis of particle size distribution for all of C3 where we transform the particle horizontal area to grain diameter expressed as ϕ. (a.) Black dots represent each particle location. (b.) Particle size distribution histogram (in sq. m). (c.) Grain diameter plotted against frequency where the red circles represent ϕ_{16} and ϕ_{84}. (d.) Frequency histogram of ϕ = -8 is the cobble-boulder transition (smaller ϕ are larger particles).

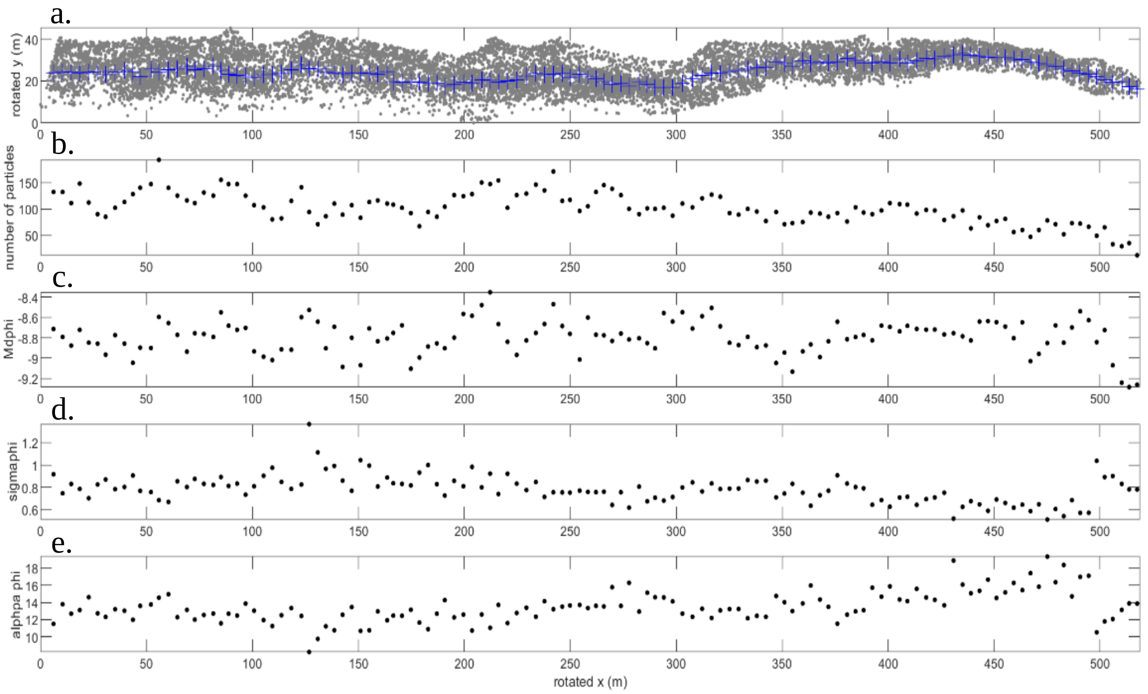

Figure 16. Sampling of grain size statistics along the scarp in C3 every 4 meters. Distance is measured along the scarp in meters and the origin is the same for all the plots. (a.) C3 rotated horizontally where gray dots represent particles, the blue crosses are in the center of each 4 m bin. (b.) Number of particles along the transect. There are 100 particles for most of the samples. (c.) The median grain size ($Md\ \phi$) along the scarp. (d.) σ_ϕ along the scarp. (e.) α_ϕ along the scarp.

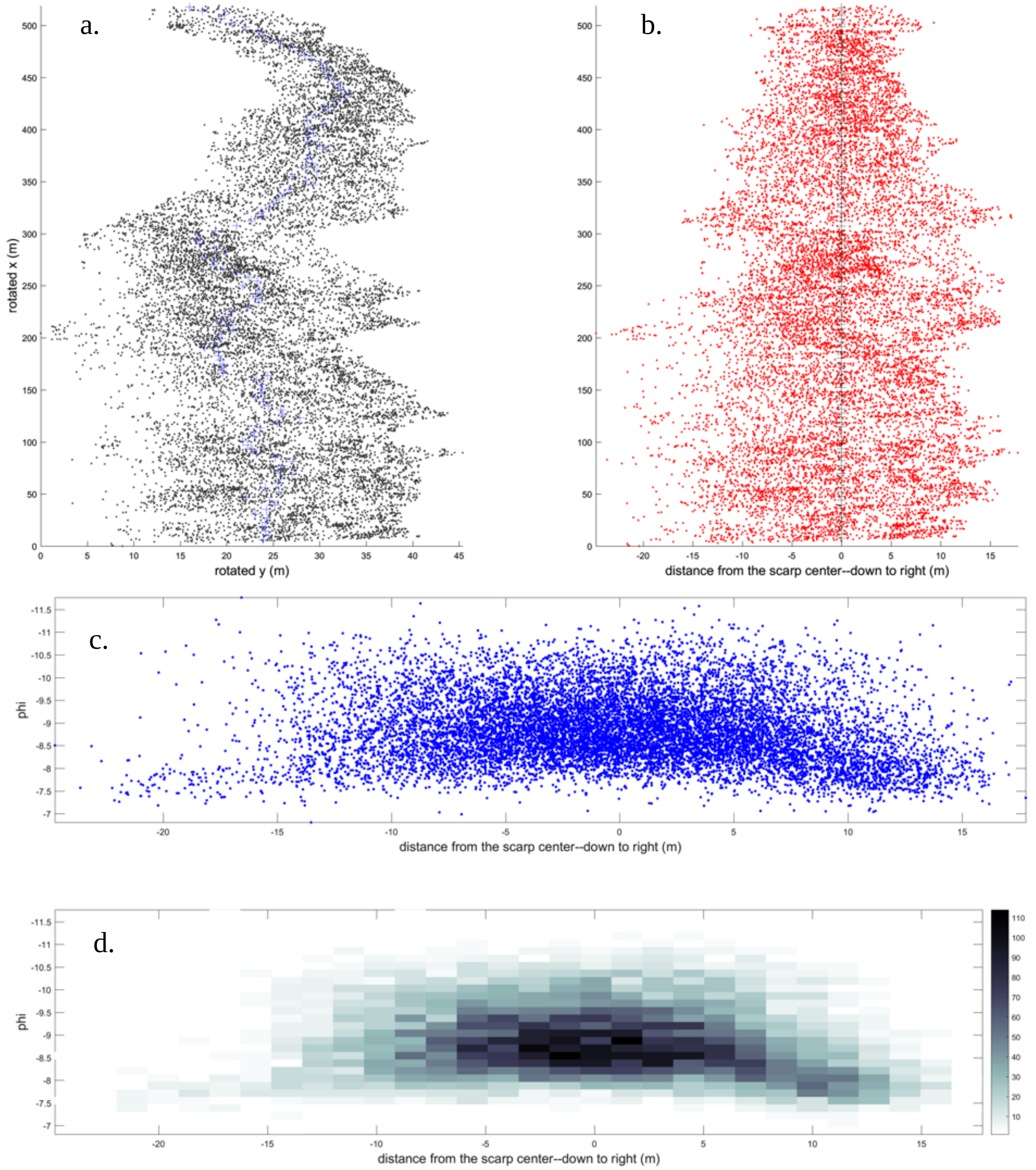

Figure 17. ϕ distribution and histogram derived from ML for C3 scarp segment. (a.) 4 m scarp sampling intervals (blue) at true center relative to particle locations. (b.) scarp center is aligned showing scarp particle distribution from center (c.) ϕ distribution looking down the adjusted scarp center (d.) ϕ histogram (particle density) looking down the adjusted scarp center.

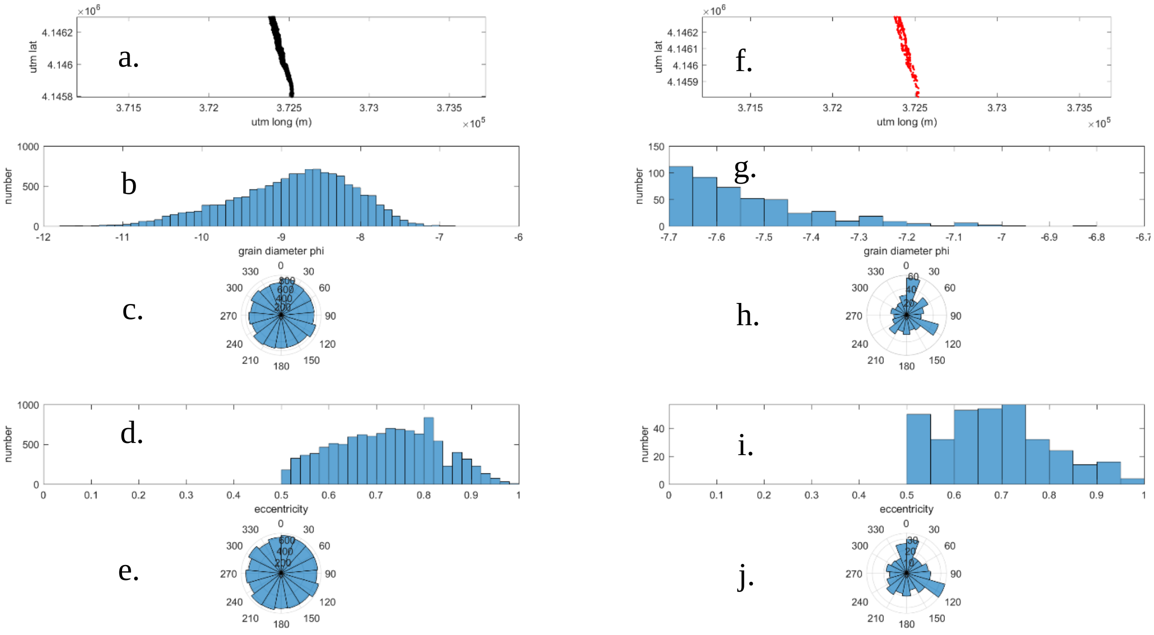

Figure 18. ϕ analysis for C3 particles (left) compared to only smaller particles where ϕ>-7.7 (right). (a.) all particle locations on C3. (b.) ϕ for all C3 particles. (c.) long axis orientations for all C3 particles. (d.) eccentricity plot for C3 particles where e>0.5. (e.) long axis orientations for Ce particles where e>0.5. (f.) particle locations on C3 where ϕ>-7-7. (g.) ϕ histogram for only smaller particles. (h.) long axis orientations for C3 particles where ϕ>-7.7. (i.) eccentricity histogram for C3 particles where e>0.5 and ϕ>-7.7. (j.) long axis orientations for particles where e>0.5 and ϕ>-7.7.

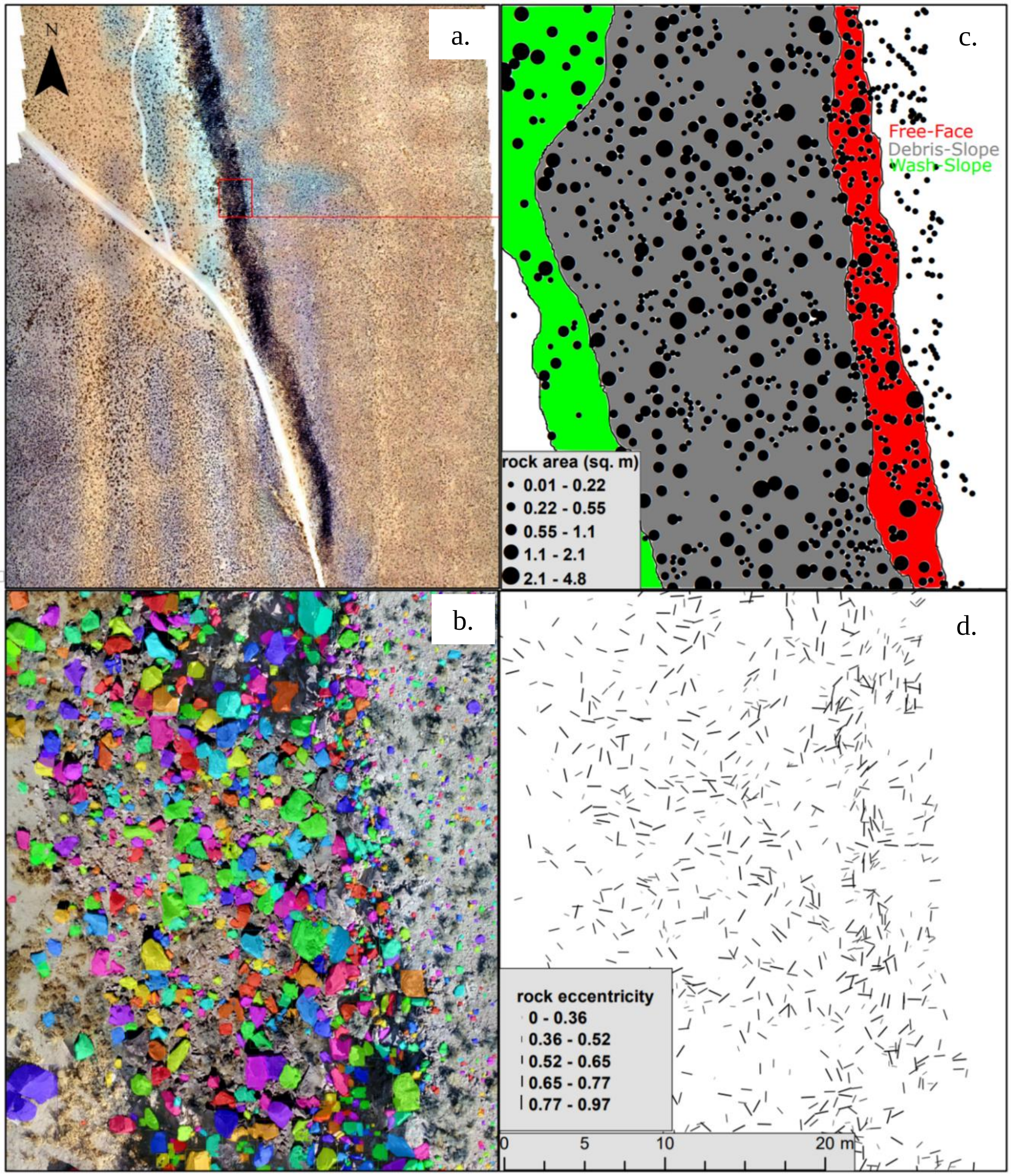
a.
N
c.
Free-Face
Debris-Slope
Wash-Slope
rock area (sq. m)
0.01 - 0.22
0.22 - 0.55
0.55 - 1.1
1.1 - 2.1
2.1 - 4.8
b.
d.
rock eccentricity
0 - 0.36
0.36 - 0.52
0.52 - 0.65
0.65 - 0.77
0.77 - 0.97
0
5
10
20 m

Figure 19. Visual and statistical information for a specific site within C3. (a.) Shows the specific site location represented by a red polygon and the background image is the orthomosaic. (b.) Machine learning mask outputs for each particle where color is for visual identification. (c.) Each dot represents a particle detected by ML and the larger the dot, the larger the particle. Additionally, the differently colored mapping units are defined by geomorphic characteristics. (d.) Each line represents a particle. The thickness of the line corresponds to the eccentricity value, where higher eccentricity produces a bolder line. The orientation of each line corresponds to the long axis orientation of each particle.

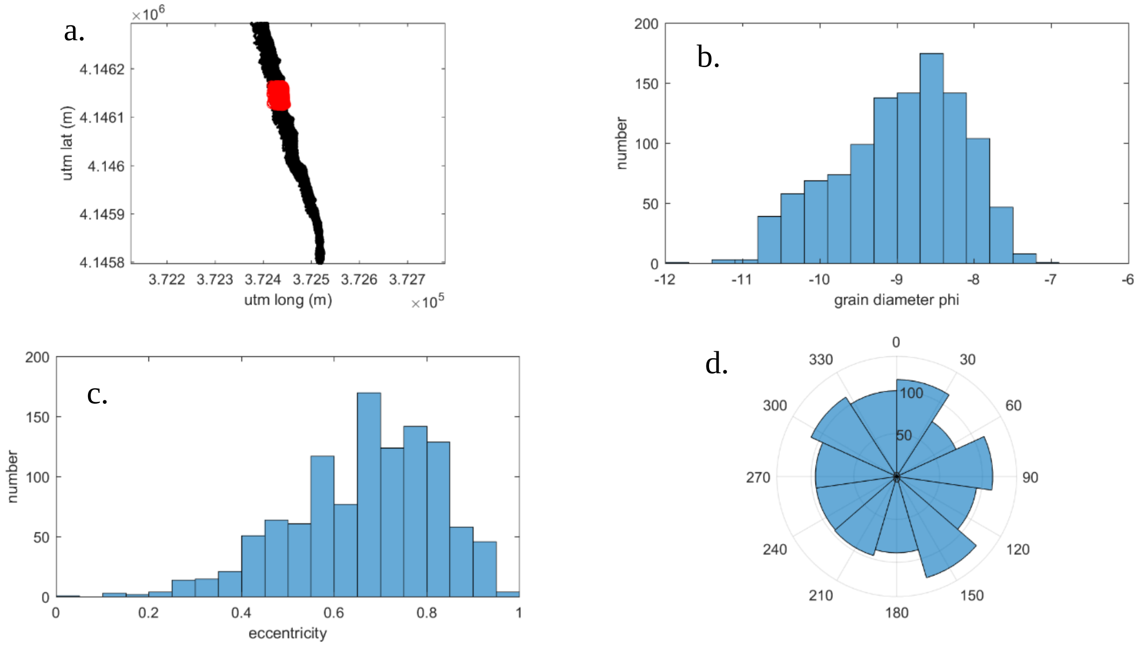
a.
×10^6
4.1462
4.1461
4.146
4.1459
4.1458
utm lat (m)
3.722
3.723
3.724
3.725
3.726
3.727
utm long (m)
×10^5
b.
200
150
100
50
0
number
-12
-11
-10
-9
-8
-7
-6
grain diameter phi
c.
200
150
100
50
0
number
0
0.2
0.4
0.6
0.8
1
eccentricity
d.
0
30
60
90
120
150
180
210
240
270
300
330
100
50

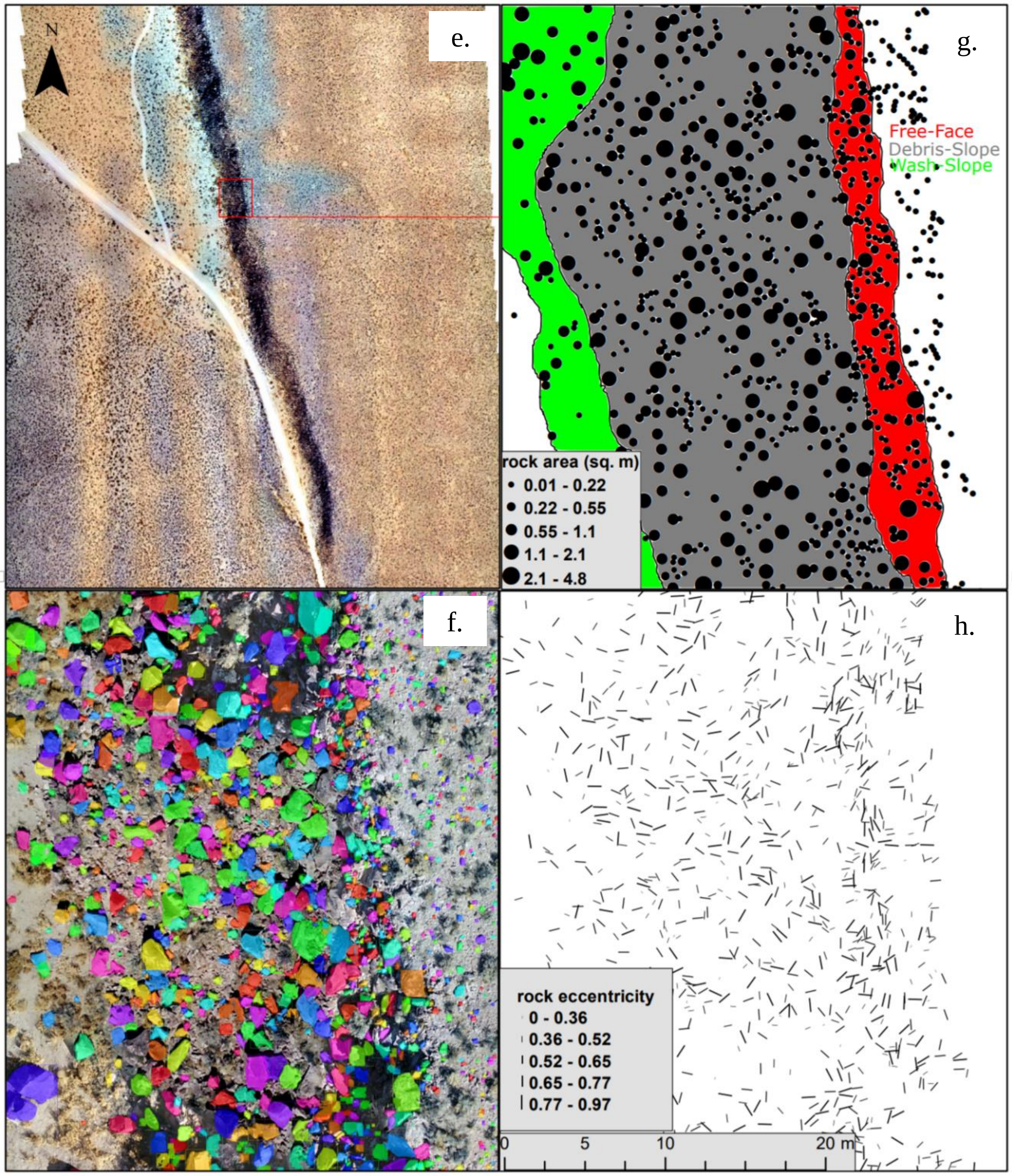
e.
N
g.
Free-Face
Debris-Slope
Wash-Slope
rock area (sq. m)
0.01 - 0.22
0.22 - 0.55
0.55 - 1.1
1.1 - 2.1
2.1 - 4.8
f.
h.
rock eccentricity
0 - 0.36
0.36 - 0.52
0.52 - 0.65
0.65 - 0.77
0.77 - 0.97
0
5
10
20 m

Figure 20. Aforementioned (Fig. 14,19) statistical analysis applied to an example portion of the scarp. This location we call a typical scarp because it is the most commonly observed geomorphic exposure of scarp segment. The typical classification is best observed in Figure 20g. with an upper resistive free-face above a wide debris-slope and even lower wash-slope. See captions for figures 14 and 19 for additional explanation.

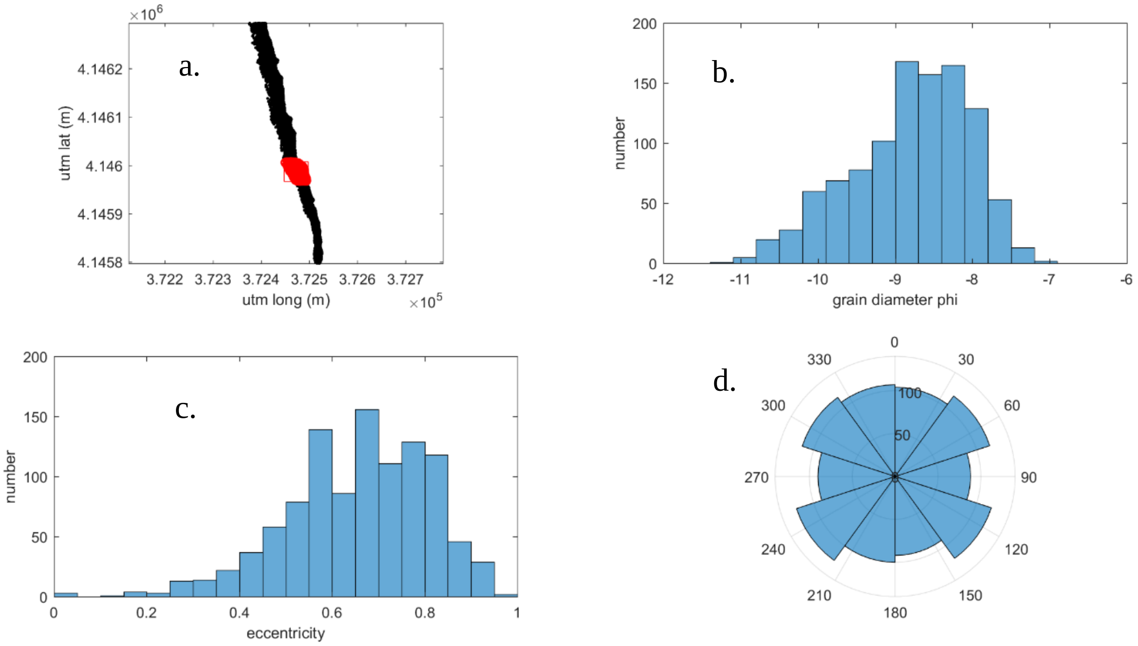
a.
×10^6
4.1462
4.1461
4.146
4.1459
4.1458
utm lat (m)
3.722
3.723
3.724
3.725
3.726
3.727
utm long (m)
×10^5
b.
200
150
100
50
0
number
-12
-11
-10
-9
-8
-7
-6
grain diameter phi
c.
200
150
100
50
0
number
0
0.2
0.4
0.6
0.8
1
eccentricity
d.
0
30
60
90
120
150
180
210
240
270
300
330
100
50

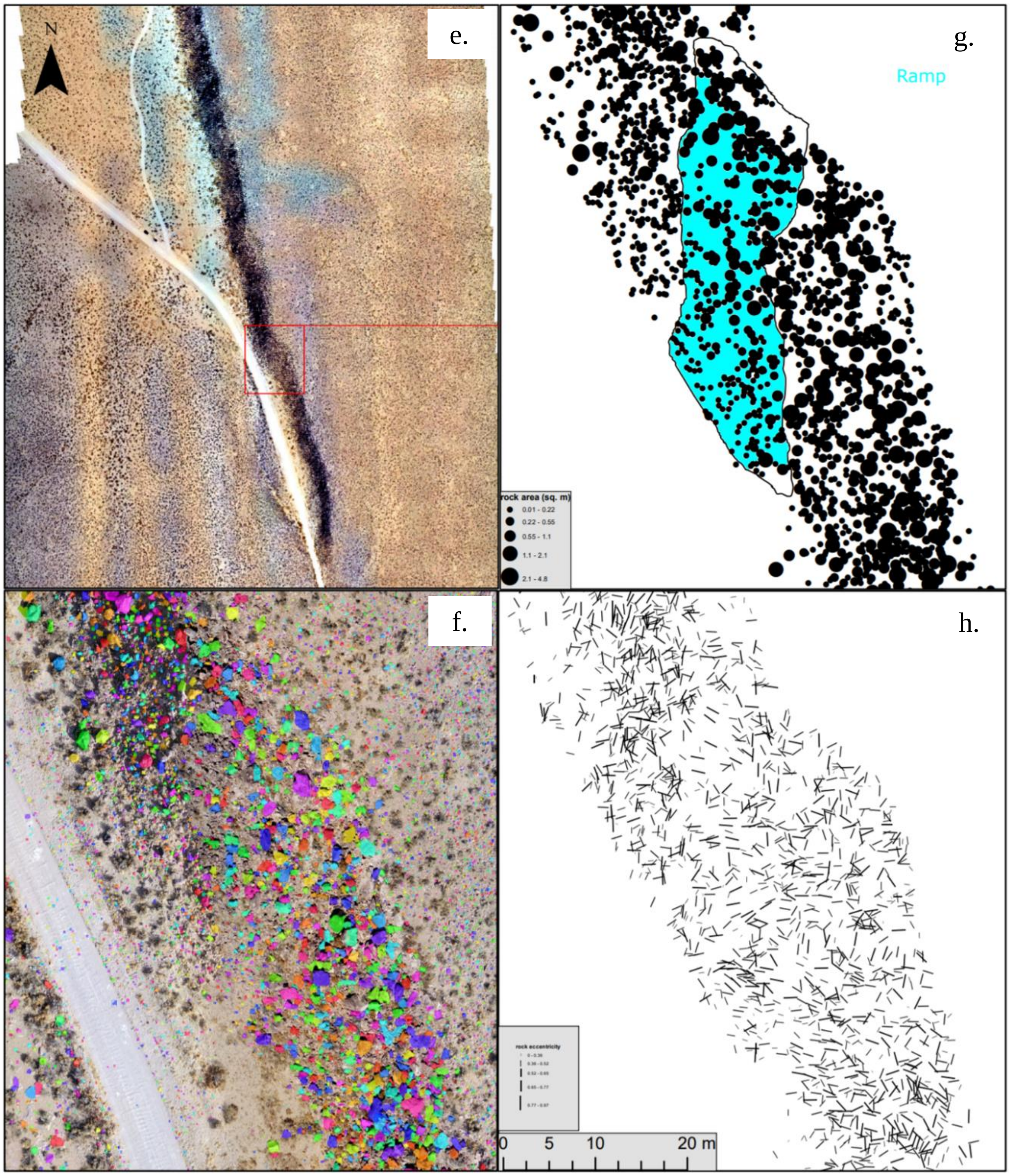
e.
N
g.
Ramp
rock area (sq. m)
0.01 - 0.22
0.22 - 0.55
0.55 - 1.1
1.1 - 2.1
2.1 - 4.8
f.
h.
rock eccentricity
0 - 0.36
0.36 - 0.52
0.52 - 0.65
0.65 - 0.77
0.77 - 0.97
0
5
10
20 m

Figure 21. Aforementioned (Fig. 14,19) statistical analysis applied to a specific site chosen by geomorphic properties. This site shows a ramp best seen in blue (Fig. 21g.) bounded by en echelon faults. A statistical standout in this analysis is two dominant long axis orientations seen in Figure 21d.

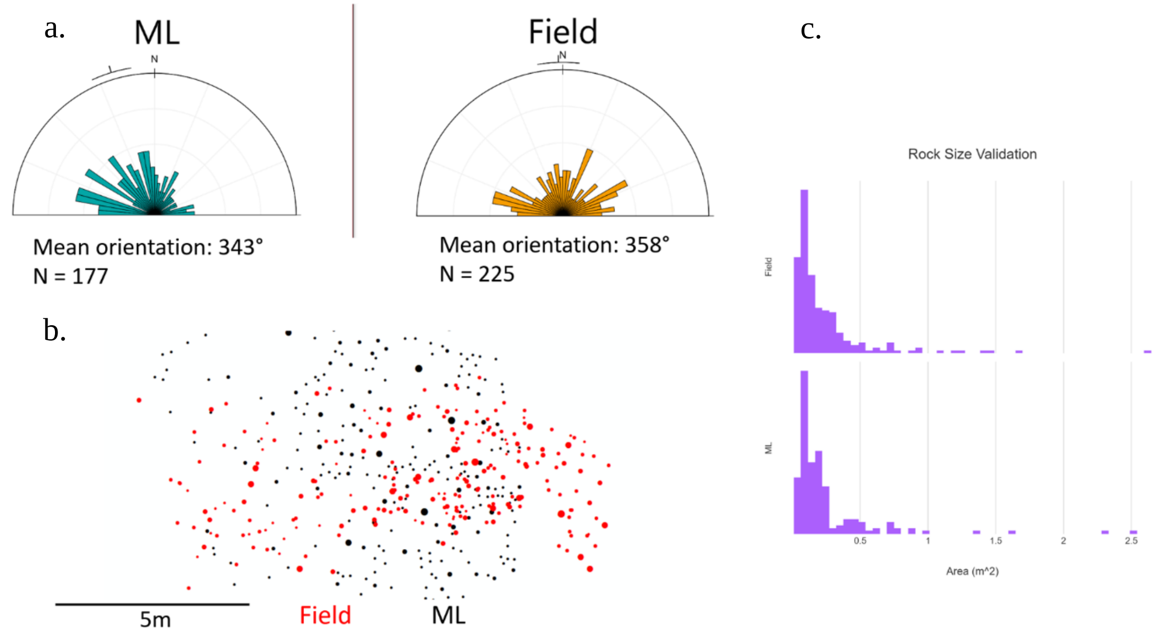

Figure 22. Comparisons of the machine learning particle traits relative to the field measured traits. (a.) Long axis orientations of particles. (b.) Dots scaled by particle area with red GPS located field measurements and black are particle centroids in the same area from the machine learning operations on the orthophotos. (c.) Rock area frequency histograms.

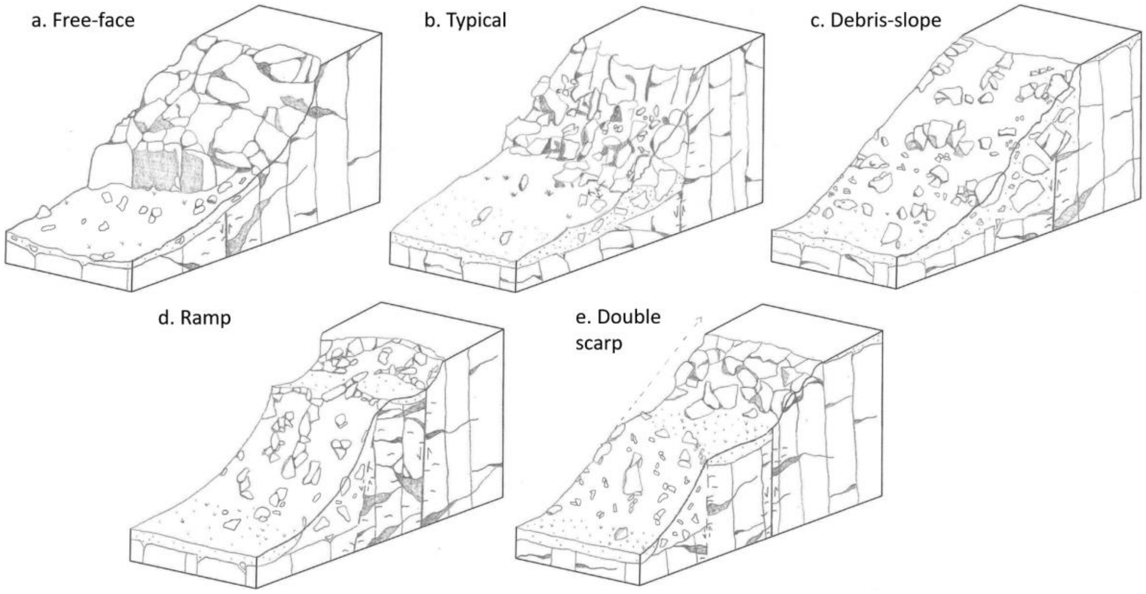

Figure 23. Conceptual models to describe rocky scarp geomorphology showing characteristics indicated by machine learning outputs and other observations from this study. (a.) The free face is primarily in situ and large particles leading to a limited particle detection by machine learning. The free-face model commonly lacks a debris slope. (b.) Typical rocky scarp is geomorphically represented by columnar joints defining the free-face that transition into a wide and poorly sorted debris slope with a low sloped base covered by wind blown dust. (c.) The debris slope exposure lacks a free-face and is composed of poorly sorted debris. (d.) The ramp model is derived from two en echelon faults merging. The merge point defines the ramp and is commonly more subdued and dust filled. The subdued ramp is possible because of the increased fracturing caused by these merging faults. (e.) This model geomorphically shows a double scarp system where the lower slope projects above the upper most exposure of the scarp. In this model, we conclude the fault has migrated from a left to right position where the left fault is no longer active, and the right fault is newly developed.

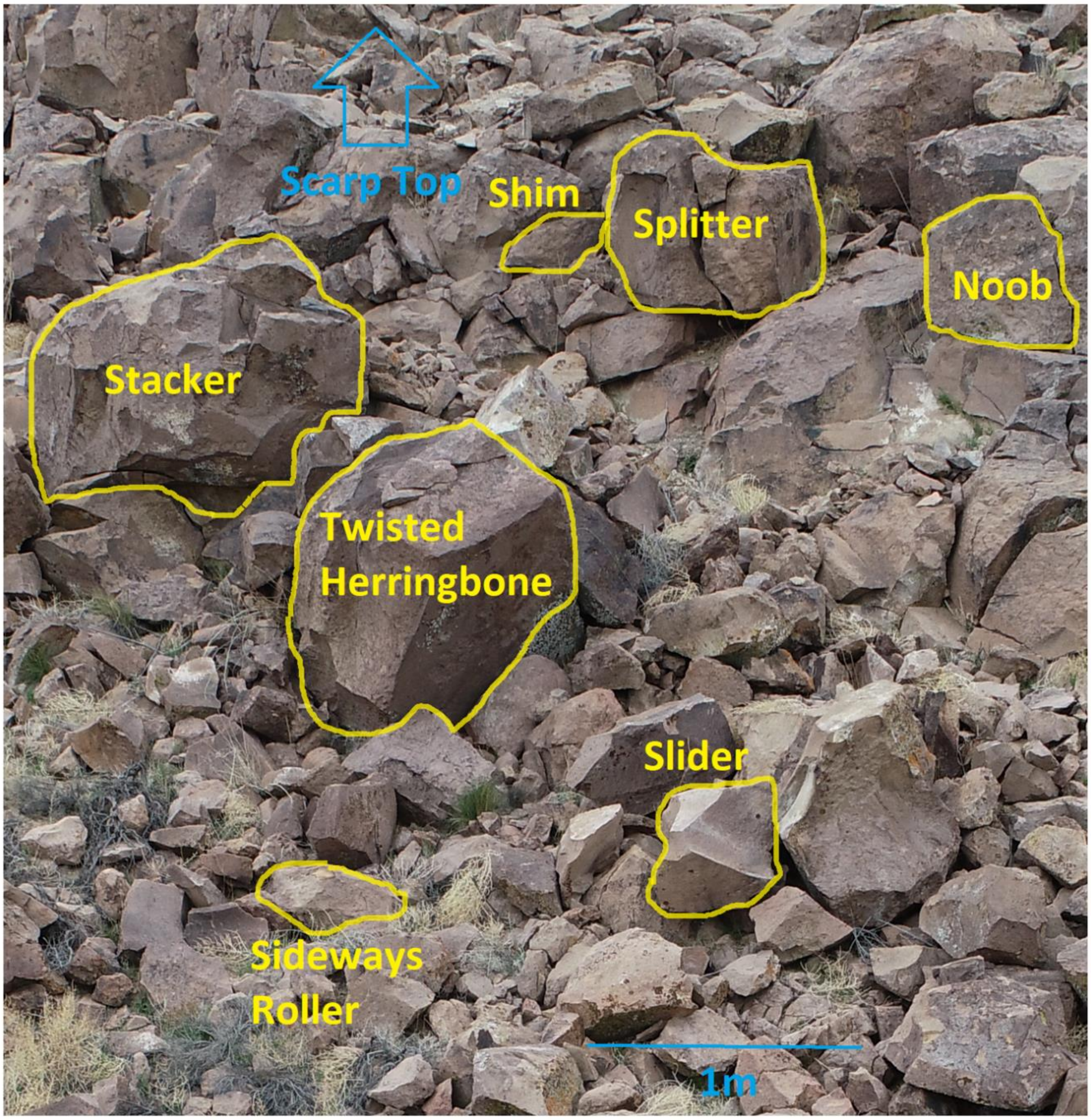

Figure 24. Updated cartoon (McCalpin, 1993, see Table 2) showing how new particles develop and transport through geomorphic processes along a rocky scarp. Shim--evolution dependent on movement of entrapping particles. Splitter--a single particle separated but not yet transported separately. Noob--a particle separated from in situ parent but not yet mobilized.

REFERENCES

Arrowsmith, J.R.A., & Pollard, D.D.P. (1996). Hillslope development in areas of active tectonics. Journal of Geophysical Research, v.101, no. B3, 6255-6275. Correction Journal of Geophysical Research}, v. 104, B1, 805, 1999

Bergen, K.J.B., Johnson, P.A.J., de Hoop, M.V.dH., & Beroza, G.C.B. (2019). Machine learning for data-driven discovery in solid Earth geoscience. Science 363, 1299, 1-12.

Cas, R.A.F.C., & Wright, J.V.W. (1988). Volcanic successions Modern and ancient. London: Chapman & Hall. (“doi:10.1007/978-0-412-44640-5”).

Chen, Z.C., Scott, T.R.S., Bearman, S.B., Anand, H.A., Keating, D.K., Scott, C.S., Arrowsmith, J.R.A., & Das, J.D. (2020). Geomorphological analysis using unpiloted aircraft systems, structure from motion, and deep learning. 2020 IEEE/RSJ International Conference on Intelligent Robots and Systems (IROS 2020).

Cole, P.D.C., Calder, E.S.C., Sparks, R.S.J.S., Clarke, A.B.C., Druitt, T.H.D., Young, S.R.Y., Herd, R.A.H., Harford, C.L.H., & Norton, G.E.N. (2002). Deposits from dome-collapse and fountain-collapse pyroclastic flows at Soufriere Hills Volcano, Montserrat. The Eruption of Soufriere Hills Volcano, Montserrat, from 1995 to 1999. 231-262.

Dawers N. H., Anders M. H., Scholz C. H. (1993). Growth of normal faults: displacement-length scaling. Geology ; 21 (12): 1107–1110.

Ferrill, D.A.F., Morris, A.P.M., McGinnis, R.N.M., Smart, K.J.S., Watson-Morris, M.J.M., & Wigginton, S.S.W. (2016). Observations on normal-fault scarp morphology and fault system evolution of the Bishop Tuff in the Volcanic Tableland, Owens Valley, California, U.S.A. Lithosphere, v.8, no.3, 238-253. (“doi:10.1130/L476.1”).

Hanks, T.C.H. (2000). The age of scarplike landforms from diffusion-equation analysis. Quaternary Geochronology: Methods and Applications, AGU Reference Shelf 4, 313-339.

Hanks, T.C.H., Bucknam, R.C.B., LaJoie, K.R.J., & Wallace, R.E.W. (1984). Modification of wave-cut and faulting-controlled landforms. Journal of Geophysical Research, v.89, no.B7, 5771-5790.

James, M.R., and Robson, S., 2012, Straightforward reconstruction of 3D surfaces and topography with a camera: Accuracy and geoscience application: Journal of Geophysical Research: Earth Surface, doi:10.1029/2011JF002289.

Johnson, K.J., Nissen, E.N., Sarpalli, S.S., Arrowsmith, J.R.A., McGarey, P.M., Scharer, K.S., Williams, P.W., & Blisniuk, K.B. (2014). Rapid mapping of ultrafine fault zone topography with structure from motion. Geosphere, v.10, no.5, 1-18. ("doi:10.1130/GES01017.1; 13 figures, 1 table").
Kaiming He et al. "Mask r-cnn". In: Proceedings of the IEEE international conference on computer vision. 2017, pp. 2961–2969.

Kettermann, M.K., Weismuller, C.W., von Hagke, C.VH., Reicherter, K.R., & Urai, J.L.U. (2019). Large near surface block rotations at normal faults of the Iceland rift: Evolution of tectonic caves and dilatancy. Geological Society of America, v. 47, 781-785.

Liu X., Chen S.W., Aditya S., Sivakumar N., Dcunha S., Qu C., Taylor C. J., Das J., Kumar V. (2018). Robust Fruit Counting: Combining Deep Learning, Tracking, and Structure
from Motion. IEEE/RSJ International Conference on Intelligent Robots and Systems (IROS 2018).

McCalpin, J.P.M., Zuchiewicz, W.Z., & Jones, L.C.A.J. (1993). Sedimentology of fault-scarp-derived colluvium from the 1983 Borah Peak rupture, central Idaho. Journal of Sedimentary Petrology, v.63, no.1, 120-130.

McFadden, L. D., Eppes M. C., Gillespie A. R., Hallet B. (2005). Physical weathering in arid landscapes due to diurnal variation in the direction of solar heating. Geological Society of America Bulletin, v. 117, no. ½, 161-173.

Nash, D.B.N. (1980). Morphologic dating of degraded normal fault scarps. Journal of Geology, v.88, 353-360.

Nash, D.B.N. (1984). Morphologic dating of fluvial terrace scarps and fault scarps near West Yellowstone, Montana. Geological Society of America Bulletin, v.95, 1413-1424.

Nicol, A.N., Walsh, J.W., Childs, C.C., & Manzocchi, T.M. (2020). The growth faults. Understanding Faults.

Peacock, D.C.P. (2002). Propagation, interaction and linkage in normal fault systems. Earth Science Reviews 58, 121-142.

Pinter, N.P. (1995). Faulting on the Volcanic Tableland, Owens Valley, California. The Journal of Geology, v.103, no.1, 73-83.

Scott, C., Lao Davila, D., Manighetti, I., Scott, T., Arrowsmith, R., Leclerc, F., Matteo, L., Dominguez, S., Malavieille, J.: Topography of Normal Faults in the Volcanic Tablelands, CA 2018. Distributed by OpenTopography. https://doi.org/10.5069/G9SF2TC5

Sheridan, M.F.S. (1970). Fuarmolic mounds and ridges of the Bishop Tuff, California. Geological Society of American Bulletin, v.81, 851-868.

Stewart, I.S.S., & Hancock, P.L.H. (1988). Normal fault zone evolution and fault scarp degradation in the Aegean region. Basin Research 1, 139-153.

Stewart, I.S.S., & Hancock, P.L.H. (1990). What is a fault scarp?. Episodes, v.13, no.4, 256-263.

Tucker, G. E., S. W. McCoy, A. C. Whittaker, G. P. Roberts, S. T. Lancaster, and R. Phillips (2011), Geomorphic significance of postglacial bedrock scarps on normal-fault footwalls, J. Geophys. Res., 116, F01022, doi:10.1029/2010JF001861.

Tucker G. E., S. W. McCoy, D. E. J. Hobley (2018). A lattice grain model of hillslope evolution. Earth Surface Dynamics, v.6, 563-582.

Wallace, R.E.W. (1977). Profiles and ages of young fault scarps, north-central Nevada. Geological Society of American Bulletin, v.88, 1267-1281.

Westoby, M.J., Brasington, J., Glasser, N.F., Hambrey, M.J., and Reynolds, J.M., 2012, “Structure-from-Motion” photogrammetry: A low-cost, effective tool for geoscience applications: Geomorphology, doi:10.1016/j.geomorph.2012.08.021.

Visher, G.S.V. (1969). Grain size distributions and depositional processes. Journal of Sedimentary Petrology, v.39, no.3, 1074-1106.

APPENDIX I

MATLAB FUNCTION FOR ANALYZING GRAIN SIZE

Appendix I

Matlab function for analyzing grain size

```
function [phi, cumulative_phi_normalize, thebincenters, median_grain_size,
phi16, phi84, sigma_phi, alpha_phi] = process_area_to_phi(arealist)
%THis function takes an input vector of particle areas in sq. m and returns the
phi
%vector as well as the statistics on it
%JRA, May 2020

%convert the grain size to phi:
equiv_dia = 2.*sqrt(arealist./pi).*1000; %assume the area of a circle and
convert to mm
phi = -log2(equiv_dia);

%median diameter:
median_grain_size = median(phi);

h=histogram(phi,'Visible','off'); %h vector gives the bins of phi


cumulative_phi = cumsum(h.BinCounts);
cumulative_phi_normalize = cumulative_phi./cumulative_phi(h.NumBins);
%normalize the cumulative phi

A = h.BinEdges+(h.BinWidth/2);
thebincenters=A(1:h.NumBins);

%now we need phi84 and phi16
tf=find(cumulative_phi_normalize<0.16);
lower_node = tf(length(tf));
phi_lower = thebincenters(lower_node);
cum_lower = cumulative_phi_normalize(lower_node);
phi_upper = thebincenters(lower_node+1);
cum_upper = cumulative_phi_normalize(lower_node+1);
dx=(phi_upper-phi_lower);
dy=(cum_upper-cum_lower);
dphi=(0.16-cum_lower)*dx/dy;
phi16=phi_lower+dphi;

tf=find(cumulative_phi_normalize>0.84);
lower_node = tf(1);
phi_lower = thebincenters(lower_node-1);
cum_lower = cumulative_phi_normalize(lower_node-1);
phi_upper = thebincenters(lower_node);
cum_upper = cumulative_phi_normalize(lower_node);
dx=(phi_upper-phi_lower);
dy=(cum_upper-cum_lower);
dphi=(0.84-cum_lower)*dx/dy;
phi84=phi_lower+dphi;

sigma_phi = (phi84-phi16)/2; %graphical standard deviation
alpha_phi = ((phi84-phi16)-median_grain_size)/sigma_phi; % first order skewness


end
```

APPENDIX II

MACHINE LEARNING OUTPUT DATA

Appendix II

Rock traits from ML: https://figshare.com/articles/dataset/scarp_c3_csv/12711947

rock id	UTM easting (m)	UTM Northing (m)	Particle horizontal area (m^2)	Orientation of long axis clockwise from north (degree)	Eccentricity (eqn. 6)
0	372441.6	4146069.4	0.110	128.3	0.69
1	372441.1	4146063.8	0.038	83.3	0.17
2	372441.1	4146064.0	0.032	90	0.02
3	372441.0	4146063.6	0.046	72.2	0.78
4	372441.5	4146063.1	0.060	91.8	0.71
5	372440.7	4146063.2	0.030	81.2	0.62
6	372441.2	4146066.5	0.192	83.9	0.71
7	372442.0	4146068.4	0.141	160.7	0.46
8	372441.9	4146069.6	0.092	81.3	0.64
9	372440.1	4146064.2	0.056	81.6	0.79
10	372438.4	4146063.8	0.025	97.3	0.66